Probabilistic modeling of tephra dispersal: Hazard assessment of a multiphase rhyolitic eruption at Tarawera, New Zealand

C. Bonadonna,[1,2] C. B. Connor,[3] B. F. Houghton,[1] L. Connor,[3]
M. Byrne,[3] A. Laing,[3] and T. K. Hincks[4]

Received 14 November 2003; revised 30 August 2004; accepted 3 December 2004; published 15 March 2005.

[1] The Tarawera Volcanic Complex comprises 11 rhyolite domes formed during five major eruptions between 17,000 B.C. and A.D. 1886, the first four of which were predominantly rhyolitic. The only historical event erupted about 2 km^3 of basaltic tephra fall (A.D. 1886). The youngest rhyolitic event erupted a tephra fall volume more than 2 times larger and covered a wider area northwest and southeast of the volcano (∼A.D. 1315 Kaharoa eruption). We have used the Kaharoa scenario to assess the tephra fall hazard from a future rhyolitic eruption at Tarawera of a similar scale. The Plinian phase of this eruption consisted of 11 discrete episodes of VEI 4. We have developed an advection-diffusion model (TEPHRA) that allows for grain size-dependent diffusion and particle density, a stratified atmosphere, particle diffusion time within the rising plume, and settling velocities that include Reynolds number variations along the particle fall. Simulations are run in parallel on multiple processors to allow a significant implementation of the physical model and a fully probabilistic analysis of inputs and outputs. TEPHRA is an example of a class of numerical models that take advantage of new computational tools to forecast hazards as conditional probabilities far in advance of future eruptions. Three different scenarios were investigated for a comprehensive tephra fall hazard assessment: upper limit scenario, eruption range scenario, and multiple eruption scenario. Hazard curves and probability maps show that the area east and northeast of Tarawera would be the most affected by a Kaharoa-type eruption.

Citation: Bonadonna, C., C. B. Connor, B. F. Houghton, L. Connor, M. Byrne, A. Laing, and T. K. Hincks (2005), Probabilistic modeling of tephra dispersal: Hazard assessment of a multiphase rhyolitic eruption at Tarawera, New Zealand, *J. Geophys. Res.*, *110*, B03203, doi:10.1029/2003JB002896.

1. Introduction

[2] Numerical models are increasingly important in geological hazard studies and risk assessments [e.g., *Aloisi et al.*, 2002; *Barberi et al.*, 1990; *Canuti et al.*, 2002; *Glaze and Self*, 1991; *Heffter and Stunder*, 1993; *Hill et al.*, 1998; *Hurst and Turner*, 1999; *Iverson et al.*, 1998; *Searcy et al.*, 1998; *Wadge et al.*, 1998]. These models are used to quantify assessments that are otherwise based on qualitative, sometimes disparate geological observations [e.g., *Newhall and Hoblitt*, 2002]. Numerical simulations (1) augment direct observations, (2) characterize better the variation and uncertainty in geologic processes that often occur on long timescales compared with the timescales of human experience, and (3) allow scientists to explore a much wider range of geological processes than is possible to observe directly. Therefore evaluating the range of possible outcomes of geologic processes, such as earthquakes, volcanic eruptions, and landslides, is best achieved using probabilistic techniques that propagate uncertainty through the analysis using stochastic simulations.

[3] This is certainly true in volcanology, a field in which hazard assessments must strive to bound the range of possible consequences of volcanic activity, drawing from the geologic record, analogy, and understanding of the physics of volcanic processes. Historically, volcanology has advanced through description of volcanic processes and their impacts (e.g., Vesuvius [*Maulucci Vivolo*, 1994]; Mount Pelee [*Lacroix*, 1904]; Nevado del Ruiz [*Chung*, 1991]). While extremely important, this approach is not sufficient for mitigation of volcanic risks and numerical simulations can be used to complement these direct observations. However, such an approach is computationally expensive, because numerical models of geologic processes are generally complex, and because a large number of simulations is required to accurately replicate the range of behaviors for natural phenomena, like volcanic eruptions. Nevertheless, recent advances in parallel computing, such as the development of the Message Passing Interface (MPI) and the advent of inexpensive computer clusters [*Sterling et*

[1]Department of Geology and Geophysics, University of Hawaii at Manoa, Honolulu, Hawaii, USA.
[2]Now at Department of Geology, University of South Florida, Tampa, Florida, USA.
[3]Department of Geology, University of South Florida, Tampa, Florida, USA.
[4]Department of Earth Sciences, University of Bristol, Bristol, UK.

0148-0227/05/2003JB002896$09.00

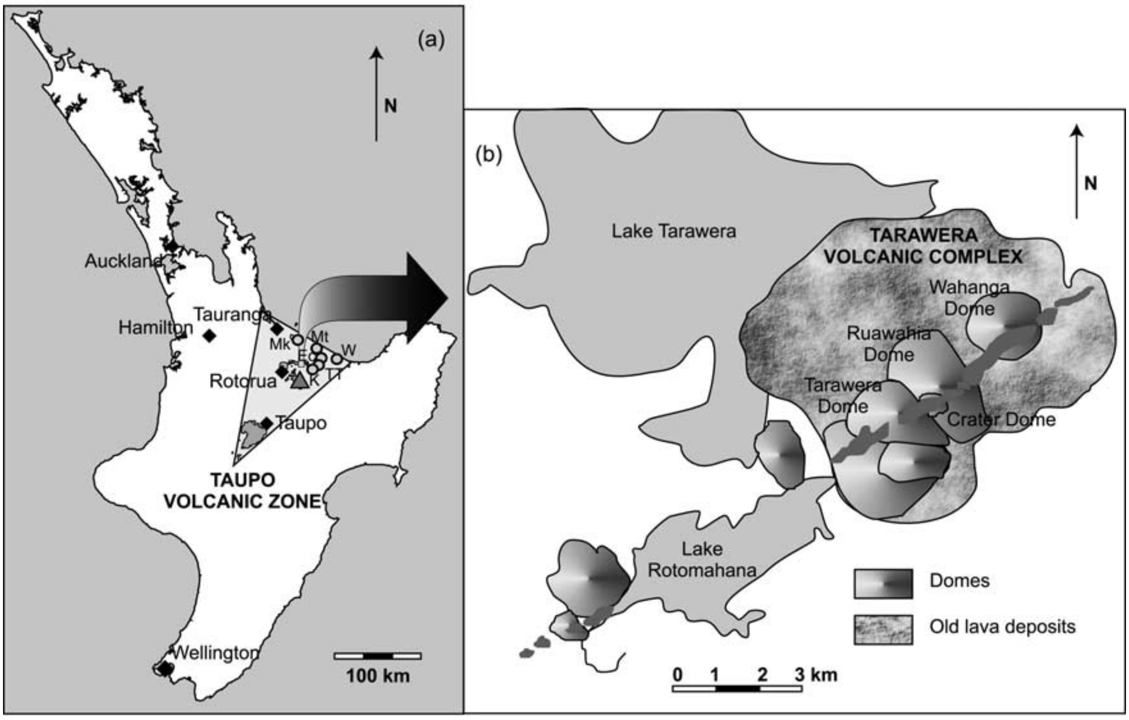

Figure 1. Map of the North Island of New Zealand showing (a) main cities (black diamonds), important populated towns (gray circles, Mk, Maketu; Mt, Matata; Ec, Edgecumbe; W, Whakatane; TT, Te Teko; K, Kawerau), Tarawera Volcanic Complex (small gray triangle) and the Taupo Volcanic Zone (large shaded triangle); (b) Tarawera Volcanic Complex (adapted from *Nairn* [1989] and *Sahetapy-Engel* [2002]) with the main domes, old lava deposits and the A.D. 1886 eruptive fissure. The names of the four lava domes produced during the ~A.D. 1315 Kaharoa eruption are also shown (only Crater Dome, Ruawahia Dome, and Wahanga Dome produced tephra fall [*Sahetapy-Engel*, 2002]). See color version of this figure in the HTML.

al., 1999], now render this approach to geological hazard assessment tractable.

[4] As a practical example, we describe the probabilistic assessment of hazards related to dispersion and accumulation of tephra fall, and, in particular, we present the tephra fall hazard assessment for Tarawera volcano (New Zealand) based on its most recent rhyolitic Plinian eruption (~A.D. 1315 Kaharoa eruption [e.g., *Nairn et al.*, 2004]). Tarawera has been one of New Zealand's most destructive volcanoes in recent times and it is famous for its basaltic Plinian eruption in A.D. 1886, which buried seven villages and killed about 150 people [*Keam*, 1988]. The ~A.D. 1315 Kaharoa eruption represents the most recent rhyolitic event in the whole Taupo Volcano Zone and produced a total tephra fall volume nearly three times larger than the A.D. 1886 eruption, covering a wider area northwest and southeast of the volcano [*Nairn et al.*, 2004; *Sahetapy-Engel*, 2002]. We have decided to assess a "Kaharoa-type" scenario to investigate the hypothetical consequences of a new rhyolitic eruption of a similar scale. On the basis of the frequency of past eruptions from this volcano complex, the annual probability of an eruption from Tarawera with volume exceeding 0.5 km^3 is $\sim 10^{-3}$ yr^{-1} [*Stirling and Wilson*, 2002], certainly a sufficiently high probability to require assessment of eruption consequences [*Woo*, 2000].

[5] This tephra fall hazard assessment is achieved through implementation of an advection-diffusion model (TEPHRA) derived from the integration of several modeling approaches and theories [*Armienti et al.*, 1988; *Bonadonna et al.*, 1998, 2002; *Bursik et al.*, 1992a; *Connor et al.*, 2001; *Macedonio et al.*, 1988; *Suzuki*, 1983]. TEPHRA is written for parallel computation on a Beowulf cluster, a networked set of personal computers running MPI. As such, TEPHRA is an example of a class of numerical models that take advantage of new computational tools to forecast hazards as conditional probabilities far in advance of future eruptions. That is, given that a scenario of volcanic activity takes place, what is the expected range of tephra fall thicknesses over a region of interest? What drives uncertainty in hazard assessment? What eruptive conditions result in hazardous tephra fall accumulations? Our goal is to illustrate how numerical models, like TEPHRA, can help resolve such questions and provide a basis for improved hazard assessment.

2. Volcanological Setting

[6] Tarawera is a dome complex within the Okataina Volcanic Centre, one of the five major calderas within the Taupo Volcanic Zone, New Zealand (Figure 1). Tarawera is made of 11 rhyolite domes and a combination of tephra fall and flow deposits that formed during five major eruptions [*Cole*, 1970; *Nairn et al.*, 2004]: (1) A.D. 1886; (2) Kaharoa, ~A.D. 1315; (3) Waiohau, ~12,000 B.P.;

(4) Rerewhakaaitu, ~15,000 B.P.; (5) eruption associated with the Okareka Ash, ~18,000 B.P.

[7] Kaharoa is the most recent rhyolitic eruption and it has been intensely studied in the last 10 years [*Leonard et al.*, 2002; *Lowe et al.*, 1998; *Nairn*, 1989; *Nairn et al.*, 2001, 2004; *Sahetapy-Engel*, 2002]. Duration of the whole Kaharoa eruption is estimated at ~4–5 years based on the corresponding lava volumes and comparisons with extrusion rates of observed dome-building eruptions [*Nairn et al.*, 2001]. However, this eruption consisted of three main phases: (1) initial phreatomagmatic explosions, (2) Plinian phase, and (3) dome extrusion [*Nairn et al.*, 2004]. Our focus is on the Plinian phase which consisted of a sequence of 11 Plinian eruptive episodes with volcano explosivity index (VEI) 4, column heights between 16 and 26 km and durations mostly between 2 and 6 hours (corresponding to units A to L [*Sahetapy-Engel*, 2002]). Unit F is characterized by the largest volume (minimum volume of 1 km^3) and highest plume (26 km) [*Sahetapy-Engel*, 2002]. These 11 Plinian eruptive episodes occurred from multiple vents, most likely Crater Dome, Ruawahia Dome and Wahanga Dome, Figure 1 [*Nairn et al.*, 2001, 2004; *Sahetapy-Engel*, 2002]).

3. TEPHRA

[8] TEPHRA consists of three main parts: (1) a physical model that describes diffusion, transport and sedimentation of volcanic particles [*Armienti et al.*, 1988; *Bonadonna et al.*, 1998, 2002; *Bursik et al.*, 1992a; *Connor et al.*, 2001; *Suzuki*, 1983]; (2) a probabilistic approach used to identify a range of input parameters for the physical model (i.e., column height; eruption duration; grain size parameters; wind profile) and to forecast a range of possible outcomes (i.e., hazard curves and probability maps); (3) a computational approach that uses parallel processing methods to speed up calculation and make fully probabilistic approaches practical.

3.1. Physical Model

[9] Particle diffusion, advection, and sedimentation are computed solving a mass conservation equation [*Armienti et al.*, 1988; *Suzuki*, 1983]. Particles of size fraction j are released from a point source i along a volcanic plume. The total mass M^0 (kg) of the eruption is

$$M^o = \sum_{i=0}^{H} \sum_{j=\phi_{\min}}^{\phi_{\max}} M^o_{i,j}, \quad (1)$$

where $M^o_{i,j}$ (kg) is the total mass fraction of particles with size j that fall from a point source i at a height z_i, H is the total height of the volcanic plume and $\phi_{\min}$ and $\phi_{\max}$ indicate the minimum and maximum particle diameter, respectively (with $\phi = -\log_2 d$, where d is the particle diameter in mm). The fraction of $M^o_{i,j}$ (kg) that accumulates on the ground at a certain point with coordinates (x, y) is $m_{i,j}(x, y)$ (kg m^{-2}), where

$$m_{i,j}(x,y) = M^0_{i,j} f_{i,j}(x,y), \quad (2)$$

with $f_{i,j}(x, y)$ (m^{-2}) a function, described in detail in the following, that uses an advection-diffusion equation to estimate the fraction of mass of a given particle size and release height to fall around the point with coordinates (x, y). Therefore the total mass M accumulated per unit area (kg m^{-2}) at a certain point on the ground (x, y) is

$$M(x,y) = \sum_{i=0}^{H} \sum_{\phi_{\min}}^{\phi_{\max}} m_{i,j}(x,y), \quad (3)$$

which is the quantity of greatest interest in forecasting volcanic hazards related to tephra fall. Thus the problem reduces to understanding the function $f_{i,j}(x, y)$, which controls the horizontal dispersion of particles, and $M^0_{i,j}$, the source term.

[10] All the particles are released instantaneously [*Armienti et al.*, 1988; *Bonadonna et al.*, 2002; *Connor et al.*, 2001; *Hurst and Turner*, 1999; *Macedonio et al.*, 1988; *Suzuki*, 1983] and are assumed to be spherical [*Bonadonna et al.*, 2002] with a settling velocity that varies according to the particle Reynolds number [*Bonadonna et al.*, 1998]. The atmosphere is divided into horizontal layers each characterized by a uniform horizontal wind velocity and direction [*Armienti et al.*, 1988; *Bonadonna et al.*, 2002; *Hurst and Turner*, 1999; *Macedonio et al.*, 1988]. Each point source i is located in a horizontal layer, and particles released from that point source are initially transported by the wind specific for that layer, until they fall into a lower layer, where they are affected by a different wind direction and velocity. This process continues until the particles reach the ground.

[11] For emission from an instantaneous point source, the analytical solution of the mass conservation equation is a Gaussian distribution of concentration in both the x and y directions [*Armienti et al.*, 1988; *Bonadonna et al.*, 2002; *Connor et al.*, 2001; *Hurst and Turner*, 1999; *Macedonio et al.*, 1988; *Suzuki*, 1983]. Particles spread horizontally due to the combined effects of turbulent eddy diffusion and gravity spreading of the plume. They are also transported by the wind for the time δt_j spent in each layer of thickness δz, with $\delta t_j = \delta z / v_j$, where v_j is the particle settling velocity. After the time δt_j, the center of the Gaussian distribution is shifted in the $x - y$ plane by a distance $\delta x_j = w_x \delta t_j$ and $\delta y_j = w_y \delta t_j$ on the axes x and y, respectively, where w_x and w_y are the horizontal components of the wind speed in that layer. Particles falling from a point source i located at (x_i, y_i, z_i) reach the ground at the time $t_{i,j}$, where

$$t_{i,j} = \sum_{\text{layers}} \delta t_j = \frac{z_i}{v_j}. \quad (4)$$

and v_j is calculated using the analytic expressions from *Kunii and Levenspiel* [1969] and modified by *Bonadonna and Phillips* [2003].

[12] As a result, the analytical solution of the mass conservation equation can be written as

$$f_{i,j}(x,y) = \frac{1}{2\pi\sigma^2_{i,j}} \exp\left\{ -\frac{\left(x - \bar{x}_{i,j}\right)^2 + \left(y - \bar{y}_{i,j}\right)^2}{2\sigma^2_{i,j}} \right\}, \quad (5)$$

where $\bar{x}_{i,j}$ and $\bar{y}_{i,j}$ are the coordinates of the center of the bivariate Gaussian distribution ($\bar{x}_{i,j} = x_i + \sum_{\text{layers}} \delta x_j$, $\bar{y}_{i,j} = y_i + \sum_{\text{layers}} \delta y_j$) and $\sigma^2_{i,j}$ is the variance of the Gaussian distribution, which is controlled by atmospheric diffusion and horizontal spreading of the plume [*Suzuki*, 1983].

3.1.1. Atmospheric Diffusion

[13] The parameter $\sigma_{i,j}^2$ controls diffusion of particles in the atmosphere. Effectively, the use of $\sigma_{i,j}^2$ in equation (5) lumps complex plume and atmospheric processes into a single parameter. This greatly simplifies the model, making it much easier to implement but also ignores processes that can affect tephra fall dispersion. For example, the diffusion coefficient is likely scale-dependent and varies with barometric pressure in the atmosphere [e.g., *Hanna et al.*, 1982]. Such factors are not considered in the model.

[14] Atmospheric turbulence is a second-order effect for coarse particles, and several models for tephra fall dispersal are based on the assumption that the atmospheric turbulence is negligible [e.g., *Bonadonna et al.*, 1998; *Bursik et al.*, 1992b; *Sparks et al.*, 1992]. However, if the fall time of particles is large, for example for ash-sized particles, atmospheric turbulence may not be negligible [*Bursik et al.*, 1992a; *Suzuki*, 1983]. For small-particle fall times, $t_{i,j}$, the diffusion is linear (Fick's law), and the variance $\sigma_{i,j}^2$ is [*Suzuki*, 1983]

$$\sigma_{\mathrm{i,j}}^2 = 4K\left(t_{i,j} + t_i'\right), \tag{6}$$

where K (m^2 s^{-1}) is a constant diffusion coefficient and t_i' (s) is the horizontal diffusion time in the vertical plume. The horizontal diffusion coefficient, K, is considered isotropic ($K = K_x = K_y$) [*Armienti et al.*, 1988; *Bonadonna et al.*, 2002; *Connor et al.*, 2001; *Hurst and Turner*, 1999; *Suzuki*, 1983]. The vertical diffusion coefficient is small above 500 m of altitude [*Pasquill*, 1974] and therefore is assumed to be negligible. The horizontal diffusion time, t_i', accounts for the change in width of the vertical plume as a function of height, which is a very complex process [*Ernst et al.*, 1996; *Woods*, 1995]. Such a change in plume width simply adds to the dispersion of tephra fall, and so can be expressed as t_i' [*Suzuki*, 1983]. Here, we approximate the radius, r_i, of the spreading plume at a given height, z_i, with the relation developed by *Bonadonna and Phillips* [2003] and based on the combination of numerical studies [*Morton et al.*, 1956] and observations of plume expansion [*Sparks and Wilson*, 1982]: $r_i = 0.34z_i$. Thus, taking $r_i = 3\sigma_p = 3\sigma_{i,j}$, where σ_p is the standard deviation of the Gaussian distribution of the mass in the ascending plume [*Sparks et al.*, 1997; *Suzuki*, 1983], and from equation (6) with $t_{i,j} = 0$ we have

$$t_i' = \frac{0.0032z_i^2}{K}. \tag{7}$$

When the particle fall time is of a scale of hours, the scale of turbulent structures that carry particles increases with time [*Suzuki*, 1983]. As an example, particles with diameter <1 mm falling from a 30-km-high plume will have an average fall time >1 hour (based on their particle settling velocity). In this case the variance $\sigma_{i,j}^2$ can be empirically determined as [*Suzuki*, 1983]

$$\sigma_{i,j}^2 = \frac{8C}{5}\left(t_{i,j} + t_i'\right)^{2.5}, \tag{8}$$

where C is the apparent eddy diffusivity determined empirically (C = 0.04 m^2 s^{-1} [*Suzuki*, 1983]). Taking $t_{i,j} = 0$ in equation (8) and $r_i = 3\sigma_{i,j} = 0.34z_i$ as for equation (7), we have that the horizontal diffusion time for fine particles is

$$t_i' = \left(0.2z_i^2\right)^{2/5}. \tag{9}$$

Figures 2a and 2c show how t_i' significantly affects the total fall time of coarse particles more than the total fall time of fine particles, i.e., ($t_{i,j} + t_i'$), because for fine particles $t_i' \ll t_{i,j}$ (Figures 2a and 2b). However, depending on the value of K, the horizontal diffusion time of coarse particles is typically smaller than the horizontal diffusion time of fine particles for low heights (Figure 2b). In this case, coarse and fine particles indicate particles with fall time less than or greater than the fall time threshold chosen as a transition between equations (6) and (8) (e.g., fall time threshold is 3600 s in Figure 2). Such a transition is not well defined based on theory but can be determined empirically.

[15] As a conclusion, once particles leave the bottom of the turbulent current, they experience different types of turbulent diffusion depending on their size. The linear diffusion described by equation (6) strongly depends on the choice of the diffusion coefficient, whereas the power law diffusion described by equation (8) strongly depends on the particle fall time and the horizontal diffusion time of the ascending plume [*Suzuki*, 1983]. If the volcanic plume is sufficiently high, some particles will experience a shift in diffusion law during fall due to the decrease in fall time (e.g., particles with diameter of 0.25 mm in Figure 2d). Figure 2d also shows the strong power law dependence of $\sigma_{i,j}^2$ on time, which makes the total diffusion more significant for fine particles.

[16] Linear diffusion and power law diffusion result in different thinning trends, with linear diffusion typically producing a thicker but narrower accumulation centered along the dispersal axis (Figure 3). Linear diffusion resembles power law diffusion in distal area only for very large diffusion coefficients (e.g., K = 100,000 m^2 s^{-1}; Figure 3a). The combination of the two diffusion laws results in a break in slope in the thinning trend which occurs at a greater distance from the eruptive vent the larger the fall time threshold (i.e., the more particle fall trajectories are described by linear diffusion; Figure 3b). This combination results in a thick and narrow deposit in proximal areas and a thinner but wider deposit in distal areas. The width of the deposit and the maximum accumulation along the dispersal axis both depend on the fall time threshold and the choice of the diffusion coefficient (Figures 3c and 3d). The differences in mass accumulation due to different fall time thresholds and to different diffusion coefficients are on the same scale (i.e., increments of 1 order of magnitude of K and FTT approximately half and double, respectively, the accumulation of tephra along the dispersal axis; Figures 3c and 3d).

3.1.2. Mass Distribution

[17] The source term, $M_{i,j}^o$, represents the distribution of mass as a function of particle size and height in the eruption column. Several methods have been used to describe particle distribution in the ascending volcanic plume [*Armienti et al.*, 1988; *Bonadonna et al.*, 2002; *Suzuki*, 1983; *Woods*, 1988].

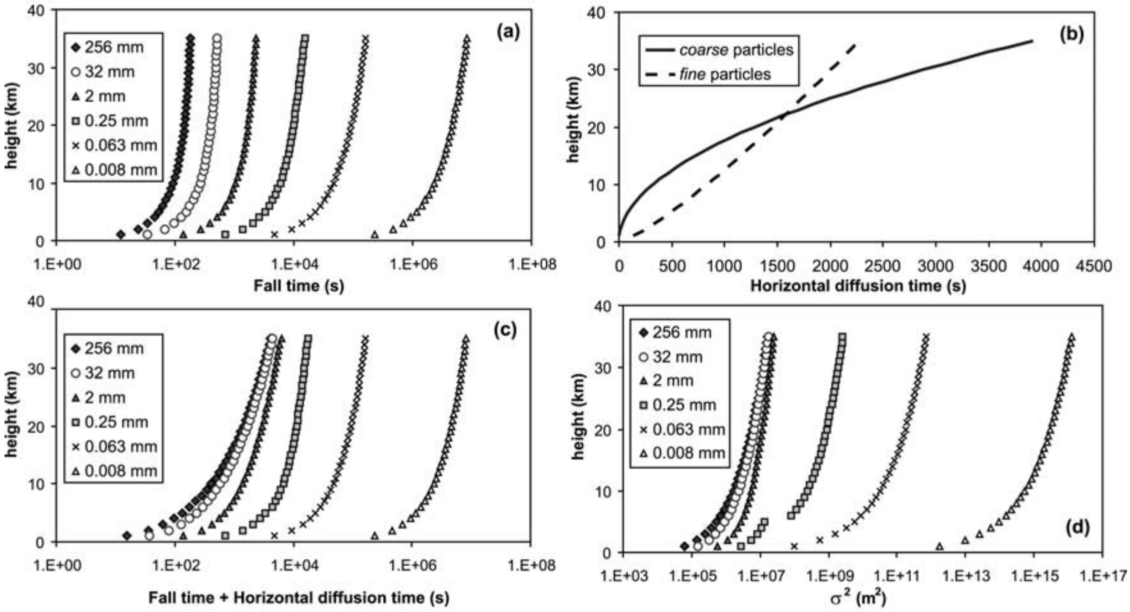

Figure 2. Plots showing the variation for different particle sizes of (a) particle fall time in the atmosphere ($t_{i,j}$) (semilog plot); (b) horizontal diffusion time in the ascending plume (t_i') (linear plot); (c) particle fall time in the atmosphere and horizontal diffusion time in the ascending plume ($t_{i,j}$ + t_i') (semilog plot); (d) variance in equations (6) and (8) ($\sigma_{i,j}^2$) (semilog plot). Calculations are done between 1 and 35 km (1 km step), with K = 1000 m^2 s^{-1} and FTT = 3600 s. Note how the plume diffusion time (t_i') mainly affects coarse particles (Figures 1a and 1c). Note also the step in $\sigma_{i,j}^2$ values at 5–6 km for 0.25-mm particles due to the shift of diffusion law (Figure 1d; equations (6) and (8)). See color version of this figure in the HTML.

[18] Here two different models are applied and compared: (1) MDM1, a uniform mass distribution along the plume (distribution 4 of *Bonadonna et al.* [2002]) and (2) MDM2, a method similar to that of *Armienti et al.* [1988] in which mass distribution is parameterized assuming a lognormal distribution in the plume as a function of a geometrical parameter, A. The parameter A controls the skewness of particle distribution in the column, regardless of particle size and terminal velocity. This model assumes that the column is well mixed and that most particles reach into the upper part of the column for A = >1. Therefore the probability density function for particle distribution as a function of height in the plume is

$$p_z(z_i) = \frac{\exp^{-\left[\frac{(\ln H)^2}{2A^2}\right]}}{AH\sqrt{2\pi}}, \qquad (10)$$

where $H > 0$ and $0 < A \leq 1$. The source term, $M^o_{i,j}$, is then calculated by assuming an eruption grain size distribution, $f_\Phi(\phi)$ [*Suzuki*, 1983]:

$$M^o_{i,j} = p_z(z_i) f_\Phi(\phi) M^o. \qquad (11)$$

3.1.3. Total Erupted Mass

[19] Given a plume height H (m), the total erupted mass M^0 (kg) is derived from an empirical power law equation [*Carey and Sigurdsson*, 1987]

$$M^o = \rho_{\mathrm{dep}} \left(\frac{H}{1670}\right)^4 \Gamma, \qquad (12)$$

where ρ_{dep} (kg m^{-3}) is the density of the tephra fall deposit and Γ (s) is the duration of the sustained phase of the eruption.

3.2. Probabilistic Determination of Inputs

3.2.1. Plume Height

[20] Either an individual plume height H or a range of plume heights can be input in TEPHRA according to the type of eruptive scenario investigated and the type of output result desired: (1) a single input value of H, together with one wind profile, is used to compute isomass maps; a single input value is also used with several wind profiles to compute hazard curves and probability maps for the worst-case eruptive episode considered (upper limit scenario, ULS); (2) a range of input values of H is randomly sampled for the computation of hazard curves and probability maps that account for the variability of eruptive episodes within a given range (eruption range scenario, ERS); and (3) a whole set of input values of H is used for the computation of cumulative probability maps, i.e., probability maps computed for a scenario of long-lasting activity (multiple eruption scenario, MES). In cases 2 and 3 any probability function of H can be sampled. We have decided to randomly sample a uniform set of values that range between log ($H_{\min}$) − log ($H_{\max}$), where $H_{\min}$ and $H_{\max}$ are the minimum and the maximum plume height observed and/or considered possible, respectively. We have chosen a logarithmic function of H to reflect a higher frequency of low plumes. As an example the distribution of plume height randomly sampled for a Kaharoa-type eruption is shown (i.e., H = 14–26 km; Figure 4a). The minimum

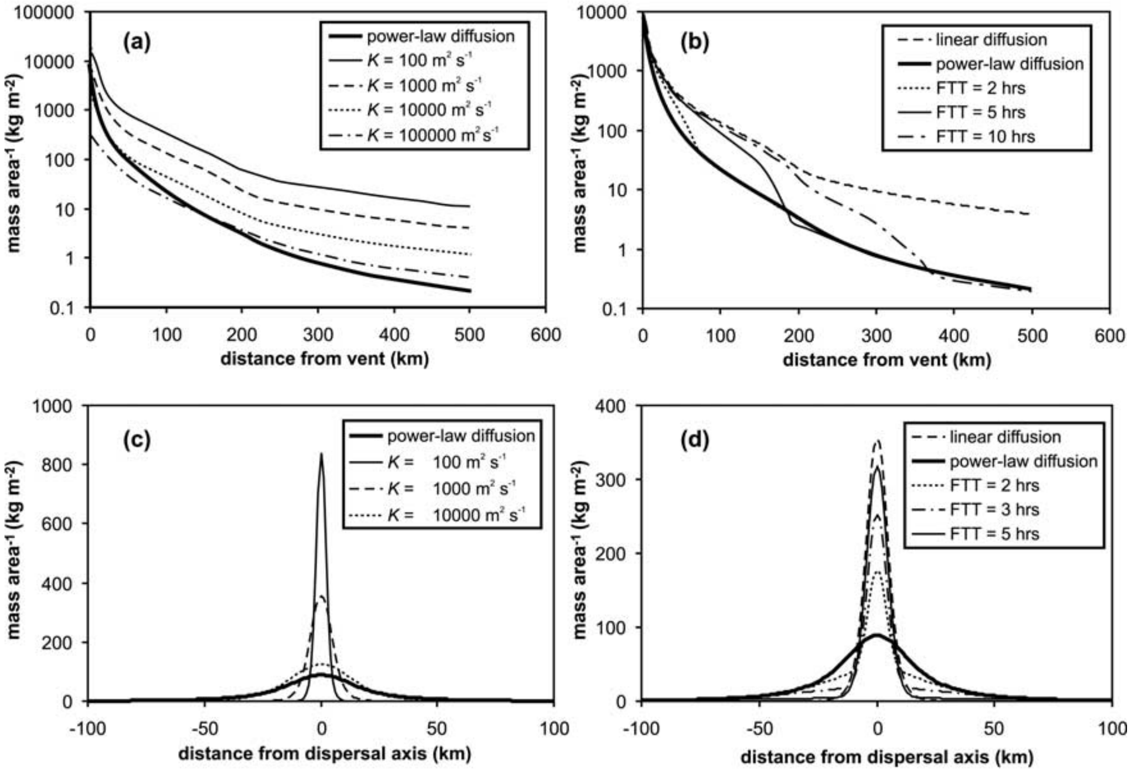

Figure 3. Semilog plots showing the computed mass per unit area along the dispersal axis for tephra fall described by (a) power law diffusion and linear diffusion with different coefficients, *K* (run 1 in Table 1); (b) linear diffusion and power law diffusion for different fall time thresholds, FTT (run 2 in Table 1). Plots of mass per unit area at a cross section taken 50 km from vent considering (c) power law diffusion and linear diffusion with different *K* (run 3 in Table 1); (d) linear diffusion and power law diffusion for different FTT (run 4 in Table 1). Diffusion of particles with fall times <FTT is described by a linear law (equation (6)), whereas diffusion of particles with fall times >FTT is described by a power law (equation (8)). 0 km in Figures 1c and 1d indicates the position of the dispersal axis.

height represents the boundary between sub-Plinian and Plinian eruptions [*Sparks et al.*, 1992] in agreement with the Kaharoa-type events, whereas the maximum height is from field data [*Sahetapy-Engel*, 2002].

3.2.2. Duration of Eruptive Episodes

[21] Together with the plume height *H*, the duration Γ of individual eruptive episodes is used to determine the total erupted mass (equation (12)). TEPHRA randomly samples the duration among a given range of values observed or considered possible. As an example, the distribution of the eruptive episode duration randomly sampled for a Kaharoa-type eruption is shown (i.e., 2–6 hours; Figure 4b).

3.2.3. Total Erupted Mass

[22] The distribution of plume height values described above, associated with the randomly sampled distribution of eruptive episode duration, results in a lognormal distribution of the total erupted mass derived using equation (12) (Figure 4c).

3.2.4. Total Grain Size Distribution

[23] A grain size distribution can be defined by expressing the corresponding minimum and maximum particle diameter, the median diameter (Md_ϕ), the graphic standard deviation (σ_ϕ) and the graphic skewness (SkG) [*Inman*, 1952]. However, the total grain size distribution of pyroclastic deposits is typically extremely difficult to determine mainly due to the methodological problems related to the integration of grain size analysis of single samples and to the scarcity of data points. As a result, only a few total grain size distributions are available [*Carey and Sigurdsson*, 1982; *Hildreth and Drake*, 1992; *Sparks et al.*, 1981; *Walker*, 1980, 1981]. Given these uncertainties, we can apply a probabilistic approach also for the determination of the grain size distribution parameters. As an example, the total grain size distribution for the ~A.D. 1305 Kaharoa eruption is not available. Therefore we have considered the total grain size distributions of three large eruptions from the Taupo Zone (i.e., Taupo, Waimihia and Hatepe Plinians [*Walker*, 1980, 1981]; Figure 5) and, in our probabilistic analysis, we have stochastically sampled Md_ϕ between -0.8 and 4ϕ (Figure 5). We have not stochastically sampled σ_ϕ, because its variation for the three distributions considered is very small (i.e., 2.3–2.9; Figure 5), and therefore we fixed it at 2.5. We have also assumed a perfect Gaussian distribution (i.e., SkG = 0).

3.2.5. Eruptive Vent

[24] The presence of multiple active vents is known for several Plinian eruptions (e.g., Tolbachik volcano [*Fedotov et al.*, 1991]; Tarawera A.D. 1886 [*Walker et al.*, 1984]; Kaharoa [*Nairn et al.*, 2001]; Rabaul [*Blong*, 1994]) and can significantly affect the patterns of tephra dispersal. Some single-vent eruptions can also occur in volcanic areas characterized by several possible future vents (e.g.,

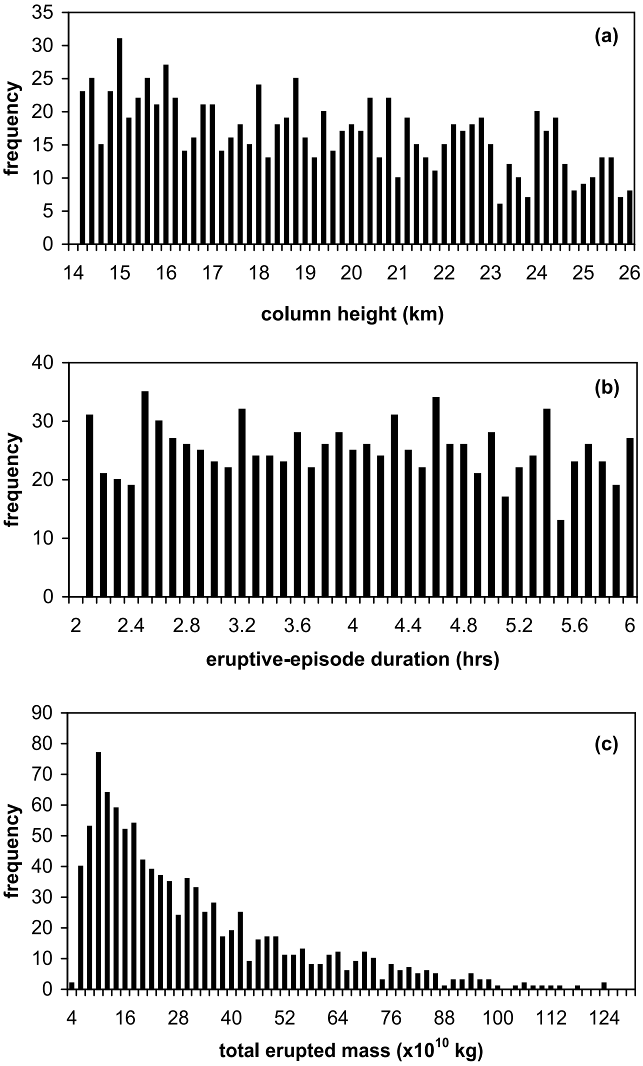

Figure 4. Frequency plots showing output results for (a) plume heights stochastically sampled between log(14 km) and log(26 km) (bin is 200 m); (b) eruptive episode duration stochastically sampled between 2 and 6 hours (bin is 0.1 hour); (c) total erupted mass determined from the combination of plume heights and eruption duration above (equation (12)) (bin is 2.00 E + 10 kg).

Auckland Volcanic Field [*Rout et al.*, 1993]; Campi Flegrei [*Di Vito et al.*, 1999]; Mount Etna [*Coltelli et al.*, 1998]; Michoacàn-Guanajuto [*Williams*, 1950]). In our hazard assessment we randomly sampled the three Kaharoa main eruptive vents (Crater Dome, Ruawahia Dome and Wahanga Dome; Figure 1).

3.2.6. Time Break Among Eruptive Episodes

[25] Given the uncertainties on the total duration of the Kaharoa eruption and the time break between individual eruptive episodes, we have decided to sample wind profiles stochastically to compute MES probability maps so that the final convergence value of probability at each grid point is independent from the time break.

3.2.7. Wind Data

[26] Wind profiles can be deterministically chosen to calibrate the model and therefore to compile isomass maps for specific eruptive events. Wind profiles can be also randomly sampled for probabilistic assessment of tephra dispersal. The wind field used by TEPHRA is stratified every 1 km. For the Tarawera assessment we have used 3 years of gridded zonal and meridional wind fields from the National Centers for Environmental Prediction Reanalysis project [*Kalnay et al.*, 1996]. The North Island of New Zealand is in the midlatitudes (~35°–41°S, New Zealand Geodetic Datum 2000); therefore winds usually blow to the east (Figure 6), and the tropopause heights are ~10 km during the winter and 15 km during the summer. Our data (1996–1998) also show a significant change in mean wind direction at relatively high altitudes (>25 km above sea level), where winds start blowing mainly to the north (Figure 6a). The direction that winds blow toward (i.e., provenance +180° in Figure 6a) varies between about −110° and 180°, and the wind velocity varies between about 2 and 40 m s^{-1} (Figure 6b). A detailed analysis of the 1996–1998 wind data shows that 86% of wind profiles have at least 15 levels of wind blowing between 0° and 180°, whereas only 3% have at least 15 levels of wind blowing between 180° and 360° (Figure 7a). Wind is more likely to blow between 180° and 360° during the austral spring-summer (i.e., September through March; Figure 7b). A frequency analysis of wind direction can give good insights and constrains on the occurrence time of past eruption by comparison with observed tephra dispersal.

4. Calibration and Validation

[27] A series of sensitivity tests were carried out to determine the best values of empirical parameters, such as the diffusion coefficient (m^2 s^{-1}), K, the fall time threshold (s), FTT, the mass distribution model, MDM, and the mass distribution parameter, A. The best fit is determined by calculating the minimum value of the misfit function (mf) keeping two parameters fixed at a time and varying the

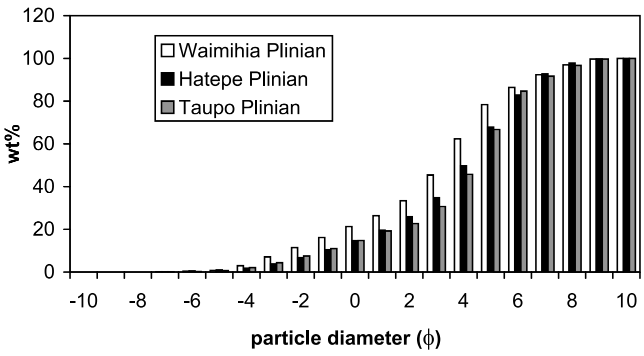

Figure 5. Cumulative plot showing the total grain size distribution of the Waimihia Plinian (white), Hatepe Plinian (black) and Taupo Plinian (gray) from *Walker* [1980, 1981]. Given that all original grain size distributions are truncated at 3ϕ, the grain size trend beyond 3ϕ is extrapolated based on a lognormal distribution. Resulting Md$_\phi$ are −0.8, 0.6 and 4ϕ, respectively. Resulting σ_ϕ are 2.3, 2.3, and 2.9, respectively.

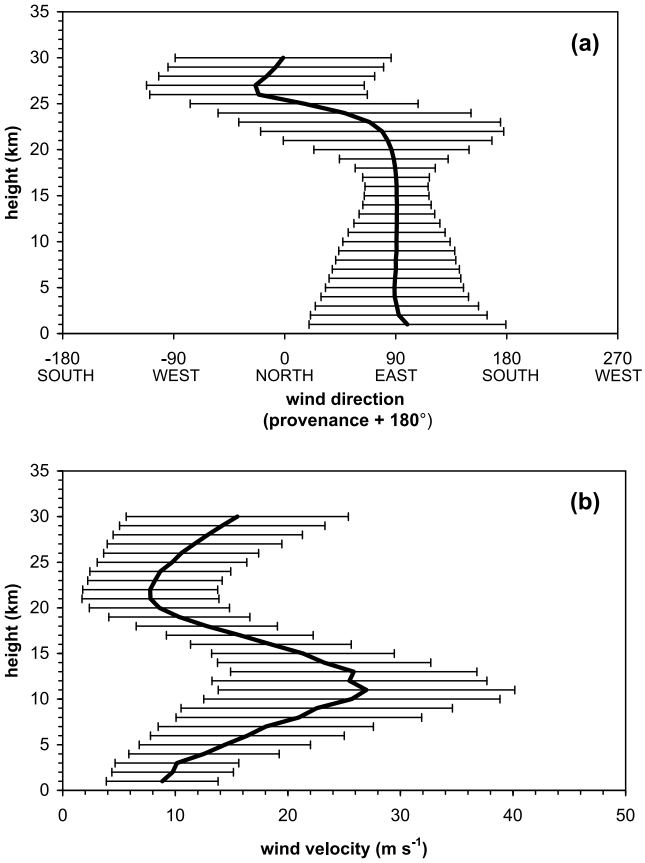

Figure 6. Plots showing (a) mean wind direction (provenance + 180°) and (b) mean wind velocity averaged every km over 3 years of wind profiles sampled 4 times a day (0000, 0600, 1200, and 1800 LT) from 1 January 1996 through 31 December 1998. The standard deviation determined for each level is also shown. These are gridded zonal and meridional wind fields from the National Centers for Environmental Prediction Reanalysis project [*Kalnay et al.*, 1996]. Data at 17 pressure levels (1000, 925, 850, 700, 600, 500, 400, 300, 250, 200, 150, 100, 70, 50, 30, 20, and 10 hPa) were interpolated linearly to 30 geopotential height levels at 1-km intervals. Values at each height level represent the average wind velocity of the four grid points surrounding the volcano.

third. The misfit function for each ground point with coordinates (x, y) is expressed as

$$mf = \sqrt{\frac{\sum_N \left(M_{obs} - M_{comp}\right)^2}{N-1}}, \qquad (13)$$

where N is the number of data and $M_{\rm obs}$ (kg m^{-2}) and $M_{\rm comp}$ (kg m^{-2}) are the observed and computed mass accumulation per unit area, respectively [*Bonadonna et al.*, 2002].

4.1. Kaharoa F (Run 5 in Table 1)

[28] Given the age of the ~A.D. 1315 Kaharoa eruption, a complete data set is not available to calibrate the model thoroughly before hazard curves and maps are computed (i.e., good mass/area data, wind data, total erupted mass, total grain size distribution). Nonetheless, we carried out sensitivity tests on the Kaharoa unit F that show a best fit for K = 10 m^2 s^{-1}, FTT = 288 s (i.e., 0.08 hours) and mass distribution model 2 with A = 1 (number of samples is 61; mass/area range is 10–450 kg m^{-2}; mf = 88.79 kg m^{-2}; Figure 8).

[29] Wind profile was chosen with a direction in agreement with the main axis of dispersal of the unit F (135°N). Maximum wind speed (27 m s^{-1}) and column height (26 km) were calculated using the method by *Carey and Sparks* [1986] [*Sahetapy-Engel*, 2002]. Total erupted mass (1.1 × 10^{12} kg) was calculated using the method by *Pyle* [1989] [*Sahetapy-Engel*, 2002]. Particle density was varied between 1000 and 2350 kg m^{-3} [*Sahetapy-Engel*, 2002]. Total grain size distribution was averaged between the Taupo, Waimihia, and Hatepe Plinian [*Walker*, 1980, 1981] (Figure 5).

[30] The misfit function is an estimate of the global agreement between observed and computed data, and so comparisons between observations and model results were also made at individual locations. Figure 8d shows the comparison between observed and computed accumulation mass (kg m^{-2}) for the "best fit" values of K, FTT, MDM and A. Computed data typically overestimates the observed data. This can be explained by the fact that the deposit was actually sampled more than 700 years after it was deposited

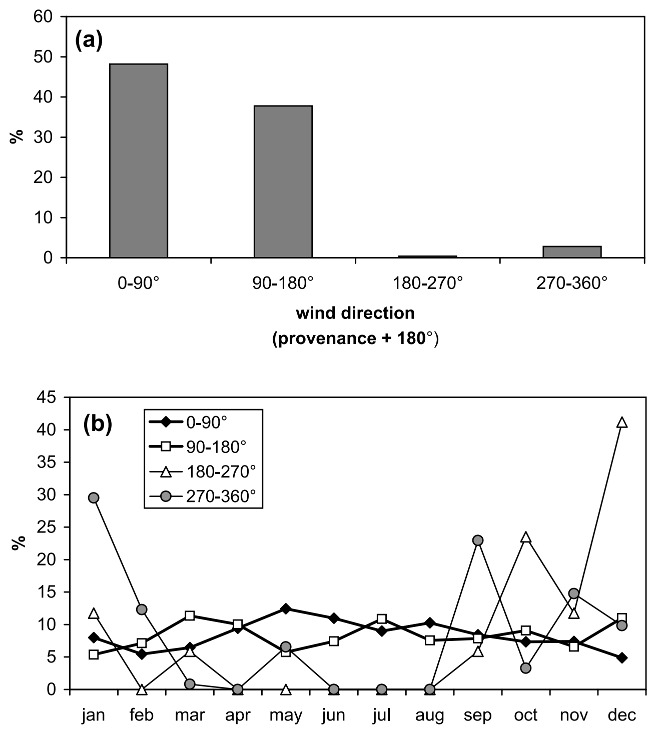

Figure 7. Plots showing (a) the percentage of wind profiles characterized by ≥15 levels with direction of provenance between 0° and 90°, 90° and 180°, 180° and 270° and 270° and 360°, respectively (degrees are from the north); (b) the percentage of such wind profiles distributed among each month. Percentages are calculated out of the total wind sample analyzed (i.e., 1996–1998; Figure 6).

Table 1. Parameters Used in the Simulations[a]

Run	Test/Scenario	Figure	Grain Size Distribution Md_ϕ	σ_ϕ	min-max ϕ	Density, kg m^{-3} Pumices	Lithics	Column Height, km	Vent Height, m	Erupted Mass, $\times 10^{10}$ kg	MDM	A	K, m^2 s^{-1}	FTT, s	Dur, hours	Winds Maximum Speed, m s^{-1}	Deposit Threshold, kg m^{-2}
Diffusion Tests																	
1	dispersal axis	3a	1.7	2.5	−7–10	1000	2350	30	1000	110	1	-	***100–100,000***	***0*** and ∞	3	WM2 (max = 10)	-
2	dispersal axis	3b	1.7	2.5	−7–10	1000	2350	30	1000	110	1	-	1000	***0–*** ∞	3	WM2 (max = 10)	-
3	cross section at 50 km	3c	1.7	2.5	−7–10	1000	2350	30	1000	110	1	-	***100–10,000***	***0*** and ∞	3	WM2 (max = 10)	-
4	cross section at 50 km	3d	1.7	2.5	−7–10	1000	2350	30	1000	110	1	-	1000	***0–*** ∞	3	WM2 (max = 10)	-
Calibration																	
5	Kaharoa F	8 and 9	1.7	2.5	−7–10	1000	2350	26.4	1000	110[b]	***1–2*** BF: 2	***0.1–1*** BF: 1	***10^{-3}–3×10^{3}*** BF: 10	***36–10,800*** BF: 288	3	Kaharoa F (max = 27)	-
6	Ruapehu	10, 11	−0.8[b]	2.4[b]	−8–10[b]	1100	2650	8.5[b]	3000	0.5[b]	***1–2*** BF: 2	***0.1–1*** BF: 1	***10^{-3}–3×10^{3}*** BF: 1	***36–10,800*** BF: 180	7v	Ruapehu[b] (max = 27)	-
Hazard Curves																	
7	ULS	12	**−0.8–4**	2.5	−7–10	1000	2350	26	1000	127	2	1	10	288	6	**1996–1998**	-
8	ERS	12	**−0.8–4**	2.5	−7–10	1000	2350	**14–26**	1000	**4–116**	2	1	10	288	**2–6**	**1996–1998**	-
Probability Maps																	
9	ULS	13a	**−0.8–4**	2.5	−7–10	1000	2350	26	1000	127	2	1	10	288	6	**1996–1998**	10
10	ERS	13b	**−0.8–4**	2.5	−7–10	1000	2350	**14–26**	1000	**4–116**	2	1	10	288	**2–6**	**1996–1998**	10
11	MES	14	**−0.8–4**	2.5	−7–10	1000	2350	**14–26**	1000	**4–116**	2	1	10	288	**2–6**	**1996–1998**	10,150
12	ULS	15a	**−0.8–4**	2.5	−7–10	1000	2350	26	1000	127	2	1	10	288	6	**1996–1998 winter**	10
13	ULS	15b	**−0.8–4**	2.5	−7–10	1000	2350	26	1000	127	2	1	10	288	6	**1996–1998 summer**	10
14	ULS	15c	**−0.8–4**	2.5	−7–10	1000	2350	26	1000	127	2	1	10	288	6	**1996–neutral**	10
15	ULS	15d	**−0.8–4**	2.5	−7–10	1000	2350	26	1000	127	2	1	10	288	6	**1997–1998 ENSO**	10

[a]Values in italic bold are the parameters varied to test the sensitivity of the model. Values in regular bold are the parameters stochastically sampled during simulations. BF is the best fit value. Grain size distribution is the total grain size distribution of the tephra fall deposit expressed with the Inman parameters (Md_ϕ and σ_ϕ [*Inman*, 1952]) and the minimum and maximum particle diameter (ϕ); grain size parameters for Ruapehu are from the 17 June 1996 deposit (run 4); grain size parameters for Kaharoa F are averaged from the grain size distributions in Figure 5 (runs 1–5); Md_ϕ for runs 7–15 is stochastically sampled between the two end-member distributions in Figure 5. Density is the measured density of the erupted centimetric clasts (kg m^{-3}); density of all pumice particles is made varied between the density of centimetric pumices and the density of centimetric lithics according to the density parameterization from *Bonadonna and Phillips* [2003]. Column height is the maximum height of the eruptive plume (km). Vent height is the height of the eruptive vent (km). Erupted mass is the total tephra fall mass erupted (kg) determined by equation (12). MDM is the mass distribution model, i.e., MDM1 is uniform distribution along the plume, and MDM2 is lognormal distribution using A. A is the mass distribution factor for MDM2. K is the diffusion coefficient (m^2 s^{-1}) (equation (6)). FTT is the fall time threshold at which the diffusion law switches between linear and power law (0 and ∞ indicate power law and linear diffusion, respectively, i.e., equations (8) and (6)). Winds are the wind profiles used in the simulations (WM2 is a wind model from *Bonadonna and Phillips* [2003] that considers linear increase of wind speed up to the tropopause level and linear decrease beyond the tropopause level; Ruapehu is the wind profile observed during the 17 June 1996 eruption [*Prata and Grant*, 2001]; Kaharoa F is the wind determined with the method of *Carey and Sparks* [1986] for the Kahaora F event with the direction along the dispersal axis of the deposit; 1996–1998 are profiles sampled 4 times a day between 1996 and 1998; 1996–1998 winter and summer are the profiles for the austral winter and summer between 1996 and 1998; 1996-neutral are the profiles for the year 1996 that was characterized by neutral conditions; 1997–1998 ENSO are profiles from 1997 to 1998 that were years characterized by El Niño-Southern Oscillation phenomenon). Dur is the duration of the eruptive episode. Deposit threshold is the hazardous threshold used to compile probability maps.

[b]Observed data.

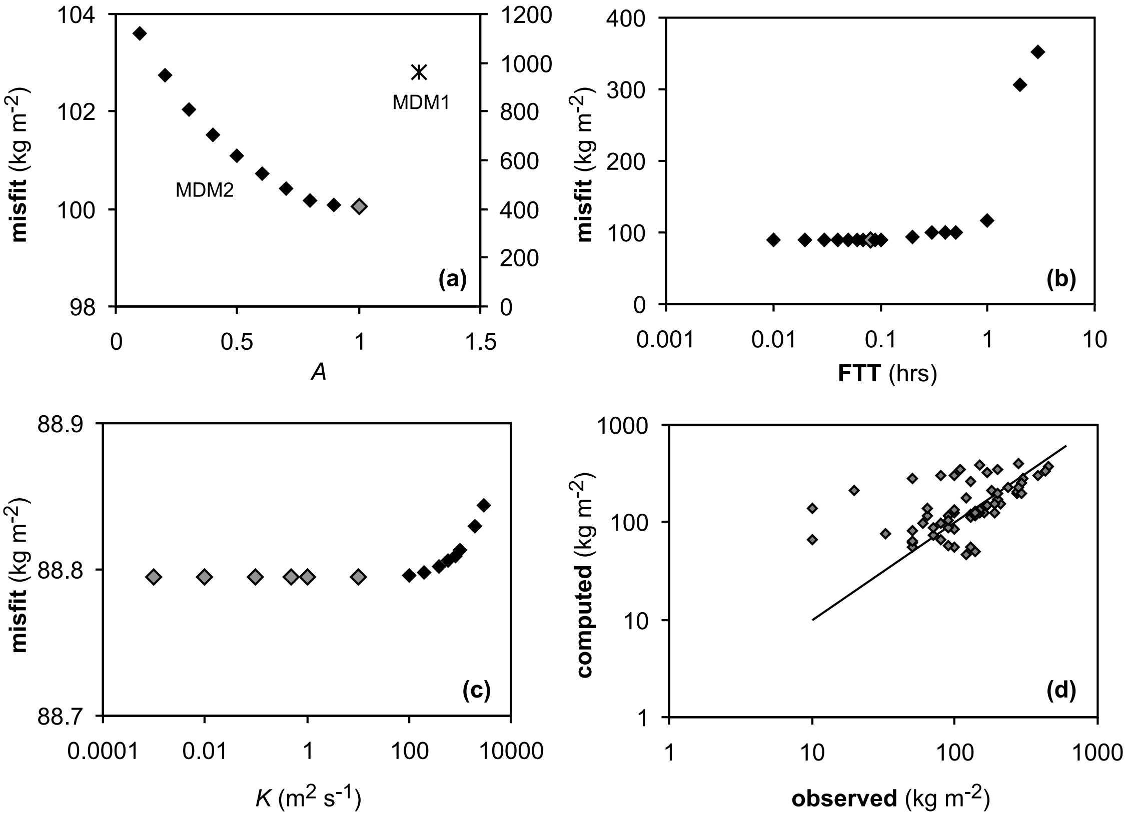

Figure 8. Plots showing the misfit function (mf; equation (13)) applied to the data set from the unit F of the Kaharoa eruption [*Sahetapy-Engel*, 2002] and calculated for (a) MDM1 (star; secondary axis) and MDM2 with different values of A (diamonds; primary axis), (b) fall time threshold, FTT and (c) diffusion coefficient, K. Minimum values of mf, i.e., best fit values, are shown in gray. (d) Log plots showing the comparison between observed data and data computed with best fit values (i.e., MDM2 with A = 1; FTT = 288 s; K = 10 m^2 s^{-1}).

[*Sahetapy-Engel*, 2002]. Figure 9 also shows a good qualitative agreement between observed and computed values but it also highlights how the quantitative comparison is limited to the medial deposit as distal data are not available.

4.2. Ruapehu (Run 6 in Table 1)

[31] In order to assess the stability of our model, sensitivity tests were also carried out on a well-studied eruption from a different volcano in New Zealand: the 17 June 1996 andesitic sub-Plinian eruption of Ruapehu. This eruption produced at least 5 $\times$ 10^9 kg of tephra fall [*Bonadonna and Houghton*, 2005]. The plume was bent over by a strong SSW wind and reached a maximum height of 8.5 km above sea level [*Prata and Grant*, 2001]. The corresponding tephra fall deposit was sampled and studied in detail [e.g., *Cronin et al.*, 1998; B. F. Houghton et al., The 17 June 1996 eruption of Ruapehu volcano, New Zealand: The anatomy of a wind-advected subplinian fall deposit, submitted to *Bulletin of Volcanology*, 2004, hereinafter referred to as Houghton et al., submitted manuscript, 2004]. Sensitivity tests carried out on the Ruapehu data set show a best fit for K = 1 m^2 s^{-1}, FTT = 180 s (i.e., 0.05 hours) and mass distribution model 2 with A = 1 (Figures 10a–10c). These best fit values are very similar to the best fit values obtained from the Kaharoa tests (runs 5 in Table 1). However, computed data show better agreement with observed data (number of samples is 114; mass/area range is 0.0002–400 kg m^{-2}; mf = 40.59 kg m^{-2}; Figure 10). It is also interesting to notice that a variation of 6 orders of magnitude of K only results in a misfit variation of 3%, and variations of 1 order of magnitude of FTT and A result in a misfit variation of 0.5% (Figures 10a–10c), showing that the algorithm is very stable.

[32] Figure 11 shows a qualitative comparison between the Ruapehu deposit computed with the best fit values and the isomass map compiled by Houghton et al. (submitted manuscript, 2004). Computed deposit beyond the first 10 km from vent shows good agreement with the observed deposit. The Ruapehu plume was pulsating and also bent over by a strong wind and, as a result the deposit shows a complicated sinuosity that cannot be accurately reproduced by a simple Gaussian model (Houghton et al., submitted manuscript, 2004). In addition, TEPHRA cannot reproduce accurately the proximal sedimentation from bent-over plumes, which are typically characterized by a very steep thinning.

[33] *Hurst and Turner* [1999] also investigated the 17 June 1996 eruption of Ruapehu using an advection-diffusion model (i.e., ASHFALL) based on the *Armienti et al.* [1988] and *Macedonio et al.* [1988] theories and models. Their best fit diffusion coefficient (6000 m^2 s^{-1}) is significantly larger than the best fit values determined for

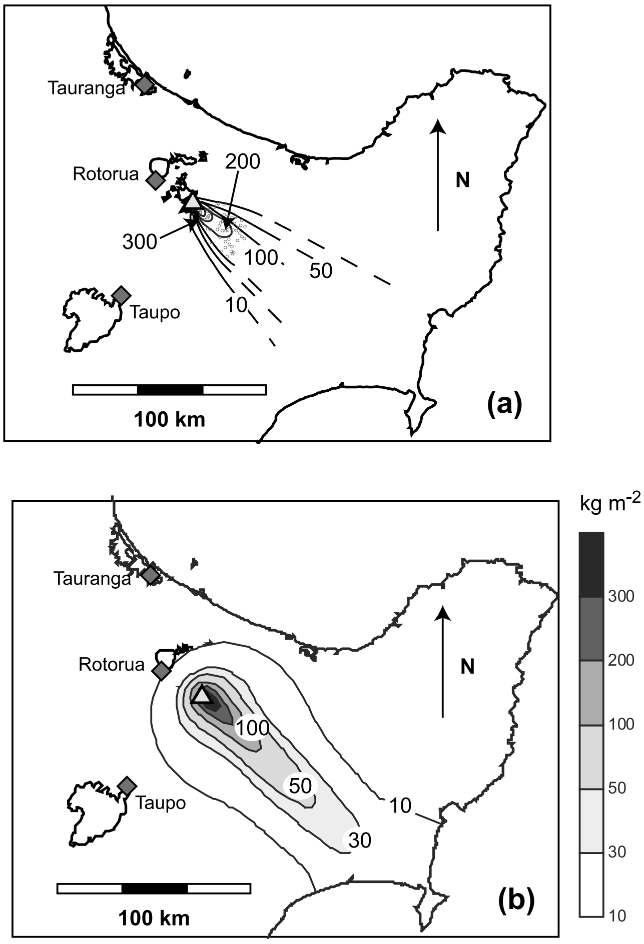

Figure 9. Comparison between isomass maps for the ~A.D. 1315 Kaharoa eruption (unit F) compiled from field data [*Sahetapy-Engel*, 2002] and the deposit computed with best fit values. The color scale is also shown (isomass contours were computed with the same interval used in the field data map). Some key cities (diamonds) and Tarawera (triangle) are shown. See color version of this figure in the HTML.

TEPHRA, mainly because ASHFALL does not account for the particle diffusion time in the plume and for the power law diffusion (see Discussion). Similarly to TEPHRA, ASHFALL does not reproduce the steep thinning in proximal areas and the pronounced sinuosity shown by the Ruapehu deposit. However, a quantitative comparison between the two models is difficult because their calibration is based on a different data set of the same deposit [i.e., *Cronin et al.*, 1998] and only a qualitative two-dimensional (2-D) comparison similar to Figure 11.

5. Probabilistic Analysis of Outputs: Hazard Assessment

[34] In our hazard assessment we have analyzed three different eruptive scenarios based on the ~A.D. 1315 Kaharoa eruption: upper limit scenario (ULS), eruption range scenario (ERS), and multiple eruption scenario (MES). These scenarios were used to compile hazard curves and probability maps. ERS hazard curves and probability maps were computed stochastically sampling 1000 different eruptions (i.e., Md_ϕ, column height, eruptive vent, eruption duration, wind profile), whereas MES probability maps were computed using 1000 sets of 10 different eruptions stochastically sampled. ULS hazard curves and probability maps were computed running 1000 eruptions with the highest plume and the longest duration. For this scenario, only Md_ϕ, the eruptive vent and the wind profile are sampled stochastically. Sensitivity tests for probabilistic analysis based on the Monte Carlo approach show that 1000 runs give a good convergence [*Bonadonna et al.*, 2002].

5.1. Hazard Curves

[35] Hazard curves considered here indicate the probability of exceeding certain values of accumulation of mass per unit area at a particular location [*Hill et al.*, 1998; *Stirling and Wilson*, 2002]. Hazard curves can be computed considering a set of eruptive episodes and a set of wind profiles.

5.2. Probability Maps

[36] Probability maps show the probability of reaching a given mass accumulation per unit area in a particular location given different sets of conditions. Different types of probability maps can be compiled depending on the specific assessment required (e.g., assessment for a specific locality; assessment for a specific area; assessment for different eruptive scenarios). For our assessment we have compiled the following.

[37] Upper limit scenario maps show the probability distribution of reaching a particular mass loading around the volcano given one eruptive episode and several wind profiles and therefore contour: $P[M(x, y) > \text{threshold} \mid \text{eruption}]$, where all eruption parameters are specified deterministically. This is useful to determine the upper limit value on tephra fall accumulation if the parameters are specified for the largest eruption considered in the scenario.

[38] Eruption range scenario maps show the probability distribution of a particular mass loading around the volcano based on the statistical distribution of possible eruptive episodes and wind profiles both sampled randomly. These maps contour: $P[M(x, y) > \text{threshold} \mid \text{eruption}]$, where all eruption parameters and wind profiles, are both sampled stochastically. The resulting map provides a fully probabilistic hazard assessment for the investigated activity scenario.

[39] Multiple-eruption scenario maps show the probability distribution of reaching a particular mass loading around the volcano given a long-lasting activity scenario (i.e., many eruptive episodes with different magnitudes) and several wind profiles contouring: $P[M(x, y) > \text{threshold} \mid \text{scenario}]$. These maps are important to assess tephra fall accumulation from multiple-phase eruptions, such as the ~A.D. 1315 Kaharoa eruption, and long-lasting eruptions, such as the 1995–1999 eruption of Montserrat [e.g., *Kokelaar*, 2002; *Sparks and Young*, 2002]. These computed probability maps assume continuous tephra fall accumulation with no erosion between eruptive episodes and are calculated using Monte Carlo simulations based on a random sampling of wind profiles [*Bonadonna et al.*, 2002].

5.3. Hazardous Deposit Thresholds

[40] In our tephra fall hazard assessment for Tarawera we have considered hazardous deposit thresholds derived from

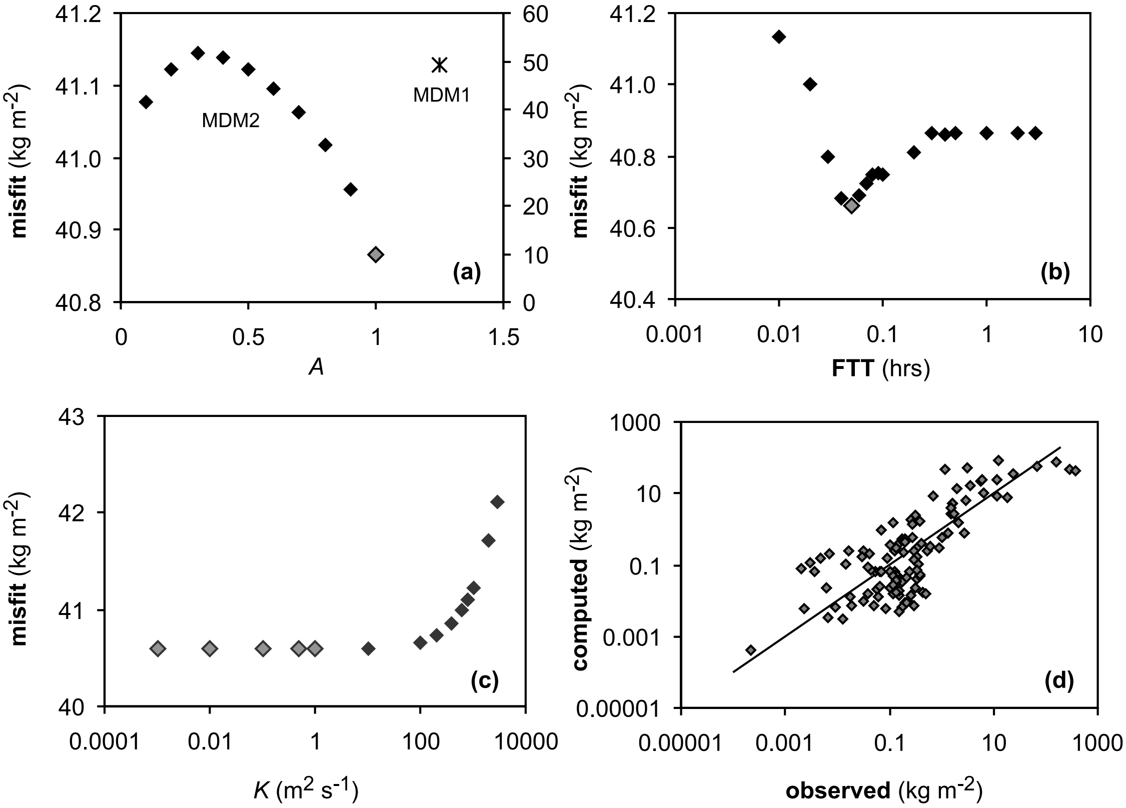

Figure 10. Plots showing the misfit function (mf; equation (13)) applied to the data set from the Ruapehu eruption (Houghton et al., submitted manuscript, 2004) and calculated for (a) MDM1 (star; secondary axis) and MDM2 with different values of A (diamonds; primary axis), (b) fall time threshold, FTT, and (c) diffusion coefficient, K. Minimum values of the mf, i.e., best fit values, are shown in gray. (d) Log plots showing the comparison between observed data and data computed with best fit values (i.e., MDM2 with $A = 1$; FTT = 180 s; $K = 1\ m^2\ s^{-1}$).

observations made on hazardous effects in New Zealand (D. Johnston, personal communication, 2004) and for a 1000 kg m^{-3} deposit density [*Sahetapy-Engel*, 2002]: 10 kg m^{-2} (i.e., ~1 cm; damage to agriculture), 150 kg m^{-2} (i.e., ~15 cm; minimum loading for roof collapse), 700 kg m^{-2} (i.e., ~70 cm; roof collapse for all buildings). However, hazard curves are also compiled to provide a general accumulation forecast at given localities independently from arbitrary hazard thresholds.

6. Hazard Assessment

6.1. Hazard Curves (Runs 7 and 8 in Table 1)

[41] Hazard curves were computed for six crucial key cities and towns: Wellington, Taupo, Tauranga, Maketu, Rotorua, Kawerau (Figure 1). The ULS hazard curves show >10% probability of reaching a tephra fall accumulation of 10 kg m^{-2} for Maketu, Kawerau and Rotorua, between 1 and 4% for Tauranga and Taupo and $\ll$0.1% for Wellington, which is characterized by very low tephra fall accumulation for all eruptive conditions considered in this assessment (Figure 12). The ERS hazard curves do not diverge significantly from the ULS hazard curves but show <2% probability of reaching a tephra fall accumulation of 10 kg m^{-2} in all localities considered except Kawerau and Rotorua (30% and 8%, respectively). All cities and town considered show $\ll$0.1% probability of reaching the minimum threshold for roof collapse (i.e., 150 kg m^{-2}) (Figure 12).

6.2. Probability Maps (Runs 9–11 in Table 1)

[42] In the case of a 26-km-high plume (ULS maps; run 9) and of a plume ranging between 14 and 26 km (ERS maps; run 10), Rotorua and the main populated towns northeast of Tarawera would be likely to receive enough tephra fall to cause damage to vegetation (30–70% and 5–40%, respectively; Figure 13). Plumes in this height range are not likely to cause roof collapse beyond the volcano (probability <1%).

[43] In the case of a multiphase eruption characterized by 10 eruptive episodes with plumes ranging between 14 and 26 km (MES maps; run 11), the main populated towns northeast of the volcano are very likely to receive enough tephra fall to cause damage to vegetation (90–100%; Figure 14a), and some could also experience collapse of the weakest buildings (e.g., Kawerau and Te Teko, 5–40%; Figure 14b). Rotorua and Maketu (north and northwest of the volcano) are also likely to experience damage to vegetation (50–80%; Figure 14a).

6.3. Seasonal Variations and Climate Fluctuations (Runs 12–17 in Table 1)

[44] The 1996–1998 wind data show that winds up to 25 km above sea level in the North Island of New

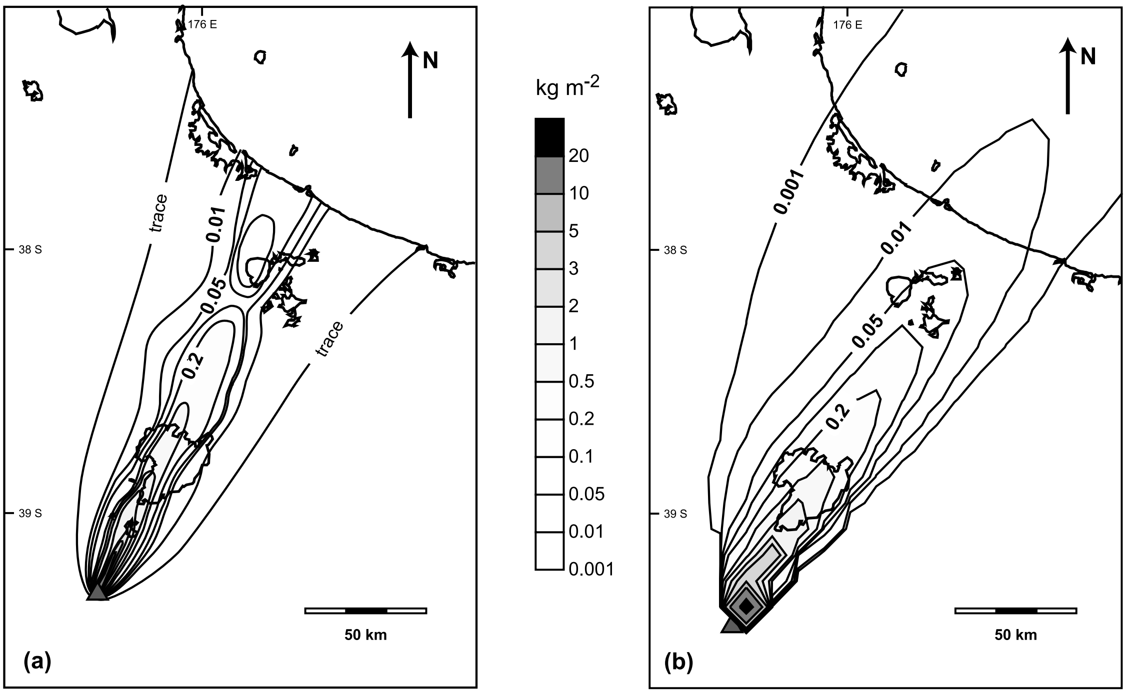

Figure 11. Comparison between isomass maps for the Ruapehu eruption (Houghton et al., submitted manuscript, 2004) and the deposit computed with best fit values. Tephra fall accumulation is in kg m^{-2}. The color scale is also shown (isomass contours were computed with the same interval used in the field data map). See color version of this figure in the HTML.

Zealand typically blow to the northeast-east-southeast (Figures 6a and 7a). Winds are more likely to blow to the northwest-west-southwest during the austral spring-summer than during the austral winter (Figure 7b). The ULS probability maps computed for a threshold of 10 kg m^{-2}, both for the austral winter (June–August; run 12) and the austral spring-summer (September–March; run 13) do not diverge significantly (Figures 15a and 15b). However, if Tarawera produces a 26-km-high plume, Rotorua is more likely to experience damage to vegetation during the summer than during the winter (about 55% and 12%, respectively; Figures 15a and 15b). The probability of reaching 10 kg m^{-2} does not vary significantly in different seasons for the populated towns north and northeast of the volcano (10–70%; Figures 15a and 15b).

[45] As also mentioned above, the New Zealand is located in the midlatitudes, and therefore is not significantly affected by ''El Niño Southern Oscillation (ENSO) phenomenon'', the major systematic global climate fluctuation that occurs at the time of an ocean warming event. However, in order to have a comprehensive wind analysis, we have chosen 3 years characterized by the main climate conditions: January 1996 to March 1997 (neutral conditions); April 1997 to May 1998 (strong El Niño); after May 1998 (La Niña). ULS probability maps computed using only wind data from 1996 (i.e., neutral conditions) and wind data only from 1997 to 1998 (i.e., ENSO conditions) do not show significant differences (runs 14 and 15; Figures 15c and 15d). As a conclusion, the winter times are the times when the area west and northwest of Tarawera would be affected the least by a Kaharoa-type eruption, regardless of ENSO phenomenon.

7. Discussion

[46] TEPHRA was born to fulfill the need for (1) implementation of existing physical models for hazard assessment of tephra fall accumulation [*Bonadonna et al.*, 2002; *Connor et al.*, 2001], (2) probabilistic determination of input and output parameters, and (3) improvement of the computational time. Numerical models used for hazard assessments of natural phenomena are typically conceptually straightforward [*Barberi et al.*, 1990; *Bonadonna et al.*, 2002; *Connor et al.*, 2001; *Hill et al.*, 1998; *Hurst and Turner*, 1999], but the application of the algorithm is made onerous by the need to execute the same calculations for several grid points (hazard map resolution) and to run numerous simulations in order to capture uncertainties in the hazard estimates (hazard map reliability). As an example, probability maps computed running 200 Monte Carlo simulations on a 450 Pentium III for a MES scenario of three years of activity at the Soufrière Hills Volcano (Montserrat, WI) would require up to 70 hours [*Bonadonna et al.*, 2002]. These long computing times are not ideal when dealing with hazard assessments required during volcanic crises. As a result, depending on the machine available, map resolution and reliability are often decreased to obtain shorter computational times. Finally, also the algorithm and the initial assumptions are often simplified to speed up the calculations (e.g., assumption of constant atmospheric density and therefore constant particle settling velocity [*Armienti et al.*, 1988; *Barberi et al.*, 1990;

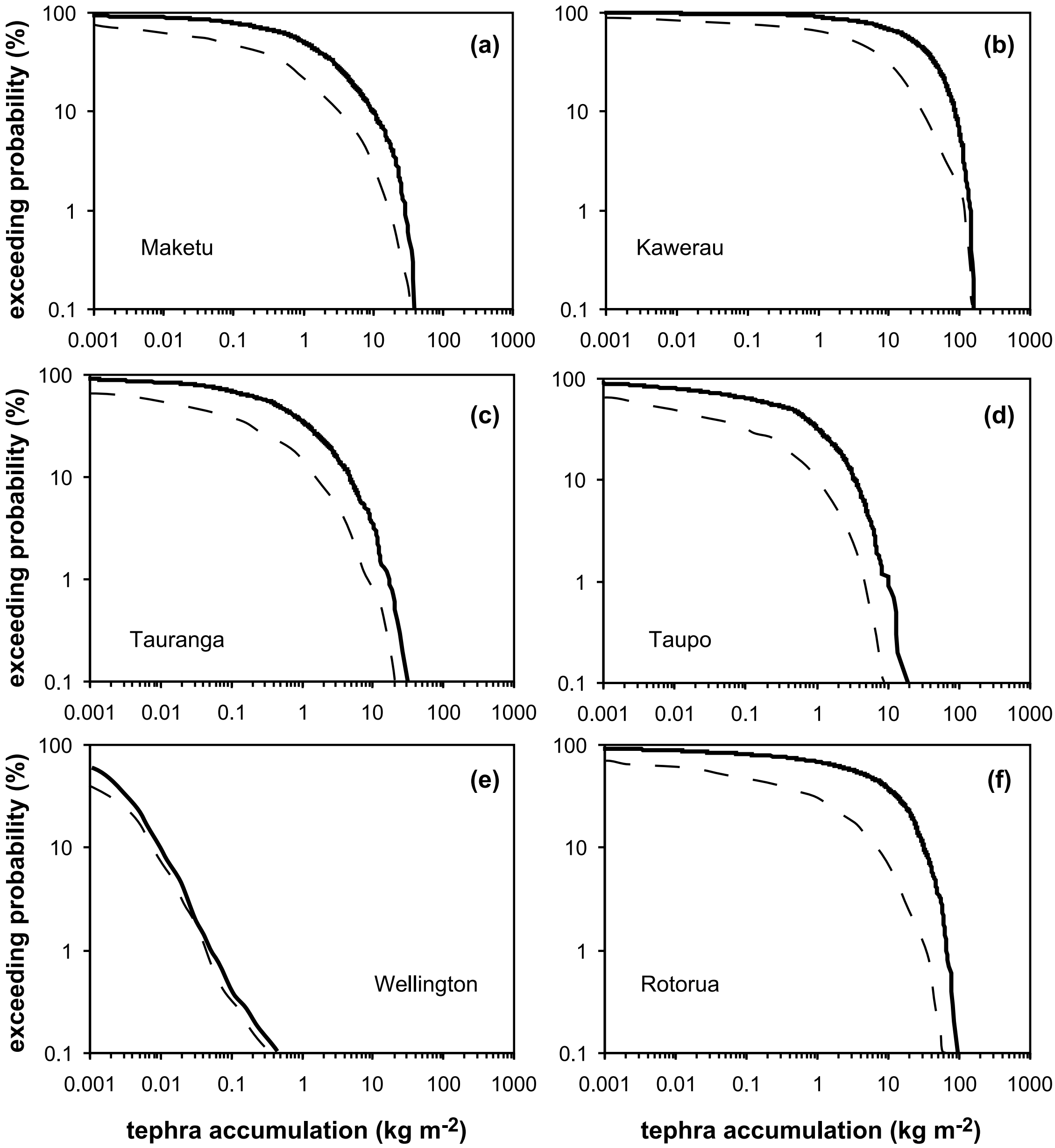

Figure 12. Hazard curves computed for the upper limit scenario (thick lines) and the eruption range scenario (dashed lines) for key cities and towns (in Figure 1): (a) Maketu, (b) Kawerau, (c) Tauranga, (d) Taupo, (e) Wellington, and (f) Rotorua. Hazard curves show the probability of exceeding a given accumulation of tephra (kg m^{-2}).

Bonadonna et al., 2002; *Macedonio et al.*, 1988]; assumption of uniform wind field [*Connor et al.*, 2001; *Hill et al.*, 1998]; assumption of a single particle diffusion law [*Armienti et al.*, 1988; *Barberi et al.*, 1990; *Bonadonna et al.*, 2002; *Connor et al.*, 2001; *Hill et al.*, 1998; *Macedonio et al.*, 1988]).

7.1. Parallelization of the Algorithm

[47] Parallelization of the algorithm represents the most efficient way to increase computing speed and therefore allowing for the implementation of the physical model and a fully probabilistic analysis of inputs and outputs. As a result, TEPHRA was designed for parallel computation on a Beowulf cluster, which usually consists of off-the-shelf personal computers connected by Ethernet, running Linux operating system, and the Message Passing Interface for parallel work. Geoscientific problems can be made parallel at a number of levels. The use of TEPHRA for hazard assessment can be defined as embarrassingly parallel because the same calculations are performed independently for a large number of input parameters and for a large number of grid points. Computation is greatly accelerated by dividing the grid points among several different computers and simultaneously performing the calculations on each. Since the solution at one grid point does not depend on the solution at any other grid point, this grid decomposition is straightforward. This type of parallel code is called a single program-multiple data model (SPMD),

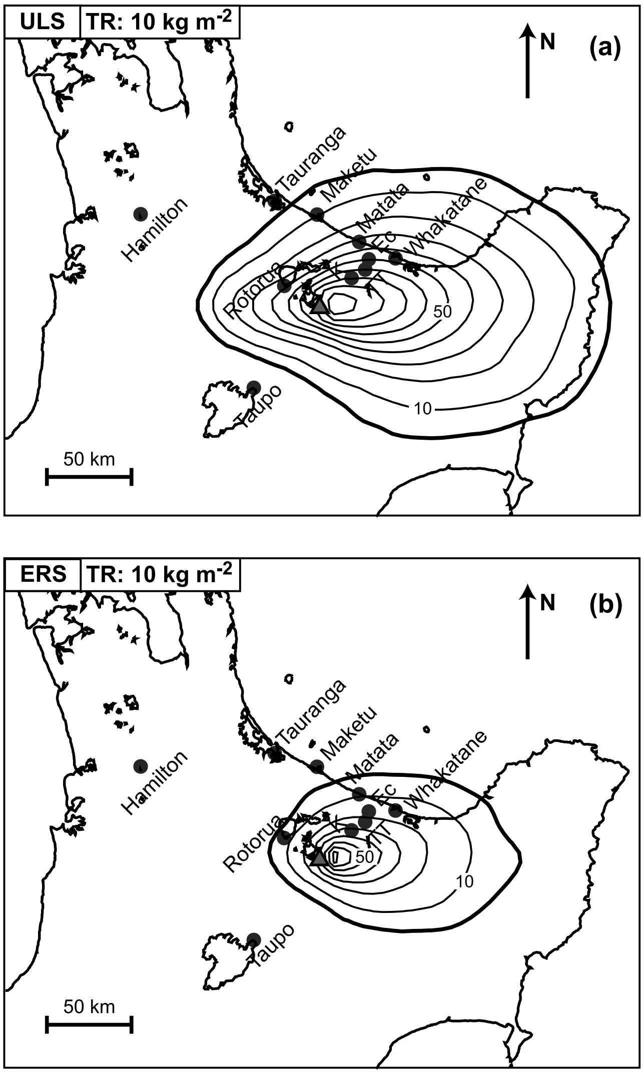

Figure 13. Probability maps run for (a) upper limit scenario and (b) eruption range scenario. Contours are spaced every 10% probability of reaching the threshold of damage to vegetation (i.e., 10 kg m^{-2}). The 5% contour is also shown (thick solid line). The map for 150 and 700 kg m^{-2} thresholds are not shown as they only show probability <1% for the populated areas around the volcano. Key cities and towns are indicated with circles, and the Tarawera Volcanic Complex is indicated with a triangle. See color version of this figure in the HTML.

because multiple instances of the same computer code run on multiple processors. In a well-implemented SPMD problem, computational speed scales with the number of nodes used.

7.2. Implementation of the Physical Model

[48] TEPHRA results from the combination of different theories and modeling approaches, representing a first step toward the integration of two main classes of tephra fall dispersal models developed during the last two decades: (1) advection-diffusion models [*Armienti et al.*, 1988; *Bonadonna et al.*, 2002; *Connor et al.*, 2001; *Glaze and Self*, 1991; *Hurst and Turner*, 1999; *Macedonio et al.*, 1988; *Suzuki*, 1983] and (2) models describing large-eddy sedimentation from plume margins combined with gravity-driven intrusion of the volcanic current at the neutral buoyancy level [*Bonadonna and Phillips*, 2003; *Bursik et al.*, 1992a, 1992b; *Ernst et al.*, 1996; *Koyaguchi and Ohno*, 2001; *Sparks et al.*, 1992].

[49] Hazard assessments are typically done using advection-diffusion models, which are mostly empirical but are designed to compile mass/area and probability maps [*Barberi et al.*, 1990; *Bonadonna et al.*, 2002; *Hill et al.*, 1998; *Hurst and Turner*, 1999]. The models from the second class are based on classic plume theory and have

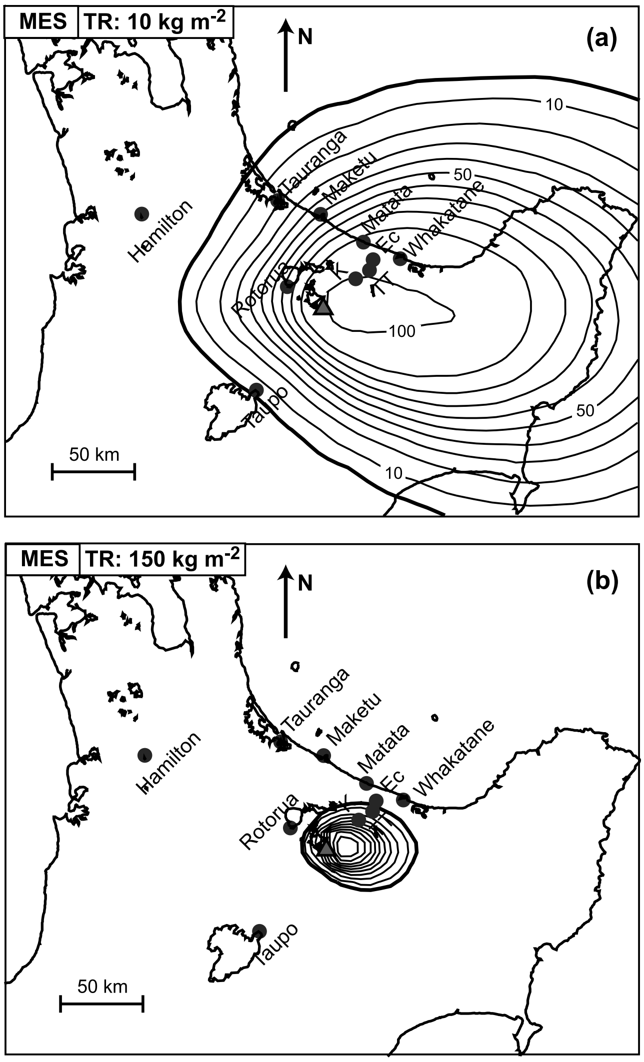

Figure 14. Multiple eruption scenario maps computed for a deposit threshold of (a) 10 kg m^{-2} (damage to vegetation) and (b) 150 kg m^{-2} (minimum loading for roof collapse). The map for a 700 kg m^{-2} threshold is not shown, as it only indicates probability <5% for most of the populated areas around the volcano. Contours are spaced every 10% probability of reaching a given threshold. The 5% contour is also shown (thick solid line). Key cities and towns are indicated with circles, and the Tarawera Volcanic Complex is indicated with a triangle. See color version of this figure in the HTML.

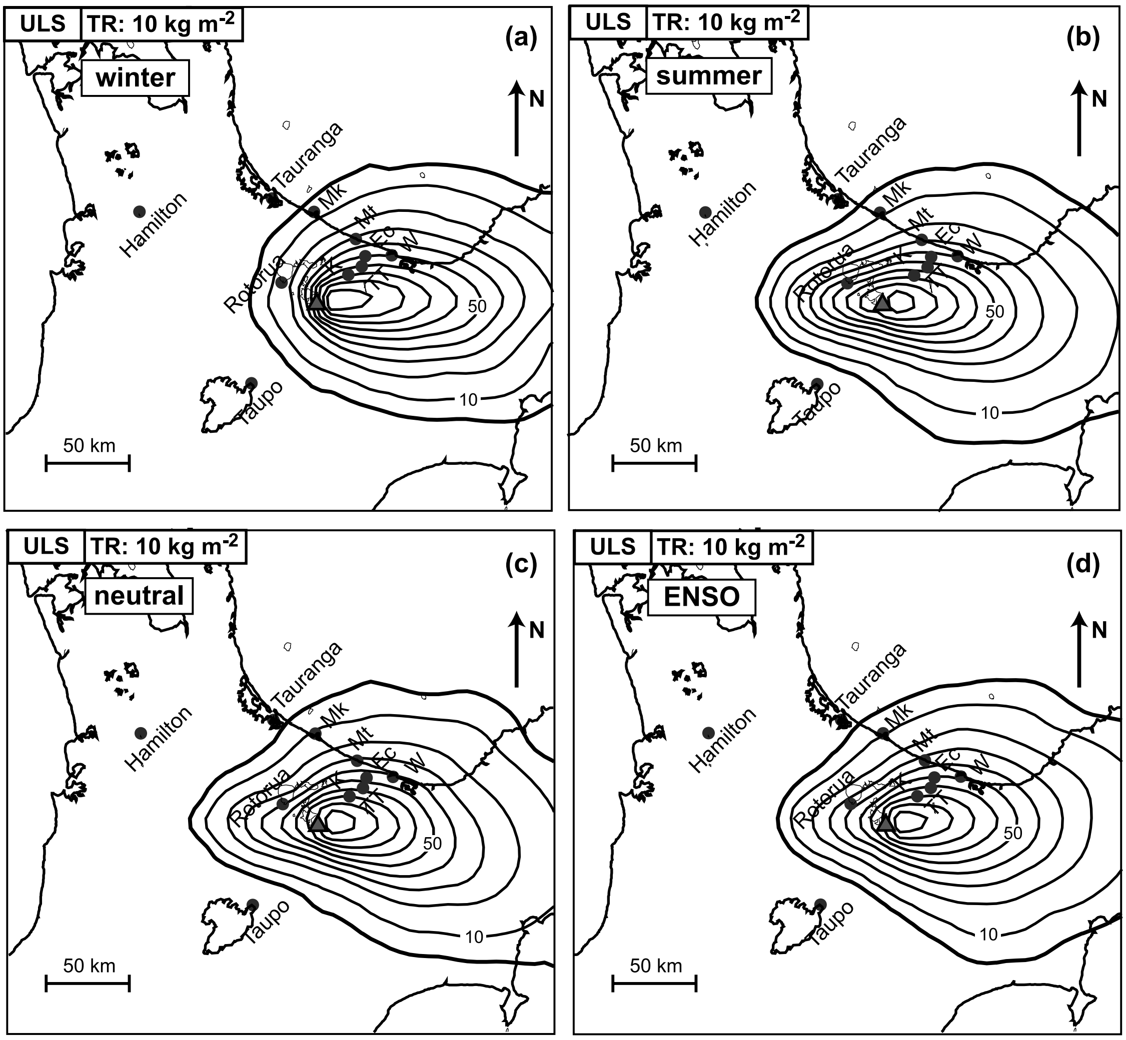

Figure 15. Upper limit scenario maps computed sampling wind data (a) from June through August (austral winter; winds mainly blowing between 0° and 180°, see Figure 7b); (b) from September to March (austral spring-summer; when winds also blow between 180° and 360°, see Figure 7b); (c) for the year 1996 (neutral conditions); and (d) from 1997 through 1998 (years characterized by El Niño-Southern Oscillation phenomenon). Contours are spaced every 10% probability of reaching the threshold for damage to vegetation (i.e., 10 kg m^{-2}). The 5% contour is also shown (thick solid line). Key cities and towns are indicated with circles, and the Tarawera Volcanic Complex is indicated with a triangle. See color version of this figure in the HTML.

mainly focused on thoroughly describing the tephra fall dynamics but have not been used to compile 2-D maps and probability assessments due to the more complex theory involved. Eventually these two classes should merge, and TEPHRA can be identified as a first step toward this direction. As an example, TEPHRA describes an instantaneous release of particles from the eruptive source, typical of advection-diffusion models [e.g., *Armienti et al.*, 1988], implemented by the horizontal diffusion time, t'_i, that accounts for the change in width of the plume as a function of height (equations (7) and (9)), derived from classic plume theory [*Morton et al.*, 1956]. This results in smaller atmospheric diffusion coefficients (e.g., diffusion coefficient of 1–10 m^2 s^{-1}), given that diffusion coefficients in advection-diffusion models typically account also for the horizontal diffusion of the plume (e.g., diffusion coefficient of 3000 m^2 s^{-1}, Vesuvius [*Macedonio et al.*, 1988]; 6000 m^2 s^{-1}, Ruapehu [*Hurst and Turner*, 1999], and 2700 m^2 s^{-1}, Montserrat [*Bonadonna et al.*, 2002]). The use of the horizontal diffusion time also results in a best fit for the plume mass distribution which is characterized by a lognormal distribution with most particles concentrated at the top. A uniform plume mass distribution gave better results for an advection-diffusion model which did not account for the horizontal diffusion time [i.e., *Bonadonna et al.*, 2002]. TEPHRA also better describes tephra fall accounting for the variation of particle Reynolds number along the particle trajectory.

[50] TEPHRA is one of the first dispersal models to account for the variation of diffusion law with particle size: (1) linear diffusion for coarse particles and (2) power law diffusion for fine particles. Diffusion is thought to be

particularly significant for settling of ash-sized particles [*Suzuki*, 1983; *Bursik et al.*, 1992a] and sensitivity tests show that the two diffusion laws result in different thinning trends (Figure 3). Very large values of diffusion coefficients could be used to simulate diffusion in distal areas (e.g., K = 100,000 m^2 s^{-1}), but they would not be consistent with diffusion coefficients typically observed for both small- and large-scale phenomena (e.g., 0–10,000 m^2 s^{-1} [*Pasquill*, 1974]) or with values typically used in advection-diffusion models (see above). The combination of two diffusion laws represents a more consistent model to describe diffusion of both small and large particles and results in a thinning break in slope. Thinning breaks in slope are commonly observed in tephra fall deposits [*Carey and Sigurdsson*, 1986; *Fierstein and Hildreth*, 1992; *Scasso et al.*, 1994; *Sparks et al.*, 1981] and are typically due to the variation of particle Reynolds number and particle aggregation [*Bonadonna and Phillips*, 2003]. However, thinning breaks in slope due to a variation of diffusion laws are feasible and could explain some discrepancies observed in computed and observed deposit thinning [*Bonadonna and Phillips*, 2003]. The cut off for diffusion law decoupling is not yet well characterized and can be only determined empirically (e.g., 180 s for the Ruapehu deposit; Figure 10).

7.3. Probabilistic Analysis

[51] Parallelization of the code not only allows the implementation of the model but also allows a fully probabilistic approach to tephra fall hazard. A stochastic sampling is used to identify input parameters for the physical model (i.e., column height; eruption duration; mass distribution parameter; grain size distribution; eruptive vent; wind profile). This is important because sometimes different eruptive scenarios need to be investigated but also because often these parameters are not well known but can be sampled from probability density functions. Therefore the more simulations are done the better the full range of possible outcomes is understood. This kind of Monte Carlo approach is very similar to the ensemble forecast technique commonly used in weather and climate forecast to deal with the uncertainties of models and/or perturbed initial conditions [*Houtekamer and Lefaivre*, 1997; *Palmer*, 2000]. Ensemble forecasting based on multiple integrations of the governing equations from perturbed or different initial conditions is inherently parallel because the exact same computations are performed many times using different input data.

[52] The tephra fall hazard assessment of Tarawera represents a typical situation: Tarawera did not produce several historical eruptions and therefore the data available for model calibration and for the identification of input parameters and eruptive scenarios are not very accurate. Furthermore, Tarawera is characterized by multiple eruptive vents and most eruptions from this volcano are characterized by multiple eruptive phases (e.g., ~A.D. 1315 Kaharoa eruption; A.D. 1886 eruption).

[53] A probabilistic approach is also used to forecast a range of possible outcomes (i.e., hazard curves and probability maps), so that the probability of exceeding certain hazardous tephra fall accumulations can be investigated for different eruptive scenarios and a wide area around the eruptive vent (Figures 12–15). The calculation of tephra fall accumulation on a grid is also inherently parallel because the exact same computations are performed many times for different grid points.

7.4. Importance of Wind Analysis

[54] TEPHRA describes the particle transport at discrete atmospheric levels (e.g., 1 km) accounting for settling velocity variations (based on particle Reynolds number variation) and wind variations (i.e., direction and velocity). The accuracy of the resulting hazard assessment is strictly related to the accuracy and number of wind profiles used and weather fluctuations analyzed. The detailed gridded zonal and meridional wind fields downloaded from the NCEP Reanalysis project allowed a full hazard assessment including specific seasonal assessments (Figures 15a and 15b) and assessments for particular climate conditions (e.g., ENSO phenomenon; Figures 15c and 15d).

[55] A good statistical study of wind profiles also helps constrain the occurrence time of a given eruption. As an example, given that the five Kaharoa units dispersed to the north and NW were produced consecutively and by plumes lower than 25 km (i.e., units H to L; plume height between 16 and 24 km [*Sahetapy-Engel*, 2002]), it is likely that these units were produced during the same austral spring-summer. This timescale of a few days to a few weeks for the Plinian phase of the Kaharoa eruption also agrees with the field observation that each unit is topped with very fine ash, possibly corresponding to the latest phase of each episode, and there is no evident sign of erosion between units. Units A–G were dispersed to the SE, and therefore it is more difficult to estimate the corresponding occurrence time, given that winds are equally likely to blow to the SE during the whole year (Figure 7). Our probabilistic analysis for the ENSO phenomenon also indicates that the unusual wind conditions that produced the Kaharoa tephra fall dispersal cannot be explained as en effect of El Niño or La Niña climate fluctuations (Figure 15d). Therefore, on the basis of purely tephra fall dispersal considerations, we can conclude the whole Kaharoa eruption could have occurred during an austral spring-summer or at least five consecutive units are very likely to have occurred during the same austral spring-summer. However, magma chamber dynamics and volcanic edifice geometry should also be considered in order to assess magma chamber recharging times and the times required to establish eruptive conditions [*Melnik*, 2000; *Pinel and Jaupart*, 2003].

7.5. Model Caveats

[56] TEPHRA represents a great extension of the existing advection-diffusion models of tephra fall dispersal. However, there are still some parameters and processes that need to be investigated and studied in more detail. First of all, advection-diffusion models are typically characterized by particle release at time 0 and therefore do not account for wind profile variations with time that can significantly affect long-lasting eruptions. An important implementation of advection-diffusion models in the frame of forecasting tephra fall dispersal for hazard assessment would be including the time factor for the simulation of tephra fall.

[57] Second, aggregation processes and particle shape effects were not accounted for in our assessment because

no corresponding data are available for the Kaharoa eruption. A reliable parameterization that can describe aggregation processes during tephra fall even when direct observations are not available would help describe tephra fall features also from those volcanoes that do not erupt very frequently and therefore do not provide detailed information of their eruptive processes. A simple parameterization of the effect of particle shape on particle settling velocity would also significantly improve the description of tephra fall dispersal. As an example, *Riley et al.* [2003] showed that the diameters of ash particles from three different distal tephra fall deposits are 10–120% larger than ideal spheres at the same terminal velocities. Unfortunately, modeling settling velocities without the assumption of spherical shape is still very complex [*Chhabra et al.*, 1999].

[58] Third, both plume mass distribution models tested (i.e., uniform and lognormal) are independent of the particle settling velocity within the plume and the plume vertical velocity. A more thorough model is needed to describe the plume dynamics.

[59] Finally, reliable data sets from powerful eruptions are needed to calibrate advection-diffusion models more accurately. Our calibration was based on one very good data set from a weak sub-Plinian plume (i.e., Ruapehu) and one poorer data set from a strong Plinian plume (i.e., Kaharoa, unit F). In order to have more reliable models for tephra fall dispersal that can provide reliable hazard assessments, we need more data sets complete with direct observations of tephra fall processes and accurate data processing.

8. Conclusions

[60] A new advection-diffusion model, TEPHRA, was developed from the combination of several theories and modeling approaches to provide an efficient and reliable tool for hazard assessment of tephra fall. After a careful analysis of the model, we can conclude make the following conclusions:

[61] 1. The main implementations of TEPHRA are (1) parallelization of the advection-diffusion code, (2) fully probabilistic assessment of input and output parameters, and (3) a more robust physical model.

[62] 2. Parallel modeling is the ideal computational approach for hazard assessment as, given the short computing times, it increases the hazard map resolution and reliability because calculations can be done on more points and because the physical models can be based on a more robust algorithm.

[63] 3. The short computing times that characterize parallel modeling also allow a fully probabilistic assessment based on (1) a stochastic sampling of input parameters and (2) a probabilistic analysis of possible outcomes.

[64] 4. A fully probabilistic approach to hazard assessment is necessary to deal with input uncertainties and different activity scenarios (i.e., Monte Carlo approach).

[65] 5. The main implementations of the physical model are (1) particle settling velocities that account for Reynolds number variations along the particle trajectory, (2) horizontal diffusion time in the volcanic plume, and (3) grain size-dependent diffusion law.

[66] 4. Linear and power law diffusion result in different thinning trends, with linear diffusion typically producing thicker but narrower deposits along the dispersal axis. The combination of the two diffusion laws results in a thinning break in slope.

[67] A combination of observations from the ~A.D. 1315 Kaharoa eruption and model simulations enabled us to evaluate probabilistically the accumulations and effects of tephra fall produced by a Kaharoa-type eruption. On the basis of our assessment we can conclude the following conclusions:

[68] Because of the prevailing winds below 25 km above sea level blowing between north and south with main direction to the east, the areas NW, west, and south of Tarawera are likely to receive little tephra fall from a Kaharoa-type eruption. Therefore key cities such as Hamilton, Auckland, and Wellington are relatively safe from hazardous tephra fall from Tarawera.

[69] 2. The most affected localities are some key towns that lie NE of Tarawera, which are likely to experience damage to vegetation in all scenario considered and also partial collapse of buildings for the MES case.

[70] 3. Detailed wind analysis shows that the dispersal of tephra fall from Tarawera is not significantly affected by El Niño or La Niña fluctuations, whereas it is slightly affected by seasonal variations, with the area immediately west of the volcano being more likely to receive tephra fall during the austral spring-summer.

[71] 4. On the basis of purely tephra fall dispersal considerations, the whole Kaharoa eruption might have occurred during an austral spring-summer or at least five consecutive units are very likely to have occurred during the same austral spring-summer.

Notation

Dimensions of each term are given in brackets: L, length; T, time; M, mass.

- A dimensionless parameter that controls the shape of the mass distribution function within the eruptive plume; equation (10).
- C apparent eddy diffusivity empirically determined (C = 0.04 m^2 s^{-1} [*Suzuki*, 1983]) [L T^{-1}]; equation (8).
- d particle diameter [L].
- $f_{i,j}(x, y)$ function of mass accumulation on the ground around a point with coordinates (x, y) (Gaussian distribution) [L^{-2}]; equation (5).
- $f_{\Phi}(\phi)$ function of total grain size distribution of the eruptive plume; equation (11).
- FTT fall time threshold [T]; diffusion of particles with fall times <FTT is described by a linear law (equation (6)), whereas diffusion of particles with fall times >FTT is described by a power law (equation (8)).
- H total plume height [L]; equation (12).
- H_{max} maximum total plume height observed and/or considered possible [L].
- H_{min} minimum total plume height observed and/or considered possible [L].
- i indices of point sources along the eruptive plume.
- j indices of particle size.
- K horizontal atmospheric diffusion coefficient ($K = K_x = K_y$) [L^2 T^{-1}]; equation (6).

K_x x component (horizontal) of the diffusion coefficient [L^2 T^{-1}].
K_y y component (horizontal) of the diffusion coefficient [L^2 T^{-1}].
K_z z component (vertical) of the diffusion coefficient [L^2 T^{-1}].
$M(x, y)$ total mass accumulated on the ground around a point of coordinates (x, y) [M L^{-2}]; equation (3).
$M^o_{i,j}$ total erupted mass of a given grain ize fraction j released from a point source i along the erupting plume [M]; equation (1).
M^o total erupted mass [M]; equations (1) and (12).
M_{comp} computed mass accumulation per unit area [M L^{-2}].
M_{obs} observed mass accumulation per unit area [M L^{-2}].
$m_{i,j}(x, y)$ mass per unit area of a given grain size fraction j released from a point source i and accumulated on the ground around a point of coordinates (x, y) [M L^{-2}]; equation (2).
Md_ϕ median diameter (grain size parameter) [*Inman*, 1952].
MDM mass distribution model: (1) uniform distribution along the eruptive plume (i.e., distribution 4 of *Bonadonna et al.* [2002]) and (2) lognormal distribution along the eruptive plume controlled by the parameter A.
mf misfit function [M L^{-2}]; equation (13).
N number of data points; equation (13).
P conditional probability.
$p_z(z_i)$ probability density function of mass distribution within the eruptive plume; equation (10).
r_i plume radius at a given height z_i [L].
SkG graphic skewness (grain size parameter) [*Inman*, 1952].
$t_{i,j}$ fall time of a particle of size j released from a point source i along the eruptive plume [T]; equation (4).
t'_i horizontal diffusion time in the volcanic plume at a point source i [T].
TR hazardous tephra accumulation threshold [M L^{-2}].
v_j particle terminal velocity of a particle of size j in the atmosphere [M L^{-1}].
w_x component of the wind speed along the x axis [L T^{-1}].
w_y component of the wind speed along the y axis [L T^{-1}].
(x, y) coordinates of a point on the ground.
(x_i, y_i, z_i) coordinates of a point source i along the eruptive plume from where particles are released.
$\bar{x}_{i,j}$ x coordinate of the center of the Gaussian distribution of mass on ground of particles of size j and released from a point i along the eruptive plume ($\bar{x}_{i,j} = x_i + \sum_{\mathrm{layers}}\delta x_j$) [L]; equation (5).
$\bar{y}_{i,j}$ y coordinate of the center of the Gaussian distribution of mass on ground of particles of size j and released from a point i along the eruptive plume ($\bar{y}_{i,j} = y_i + \sum_{\mathrm{layers}}\delta y_j$) [L]; equation (5).
z_i height of a point source i along the eruptive plume [L].
Γ duration of the Plinian discharge [T]; equation (12).
δt_j time spent by a particle of size j within each atmospheric layer [T].
δx_j wind transport of a particle of size j along the x axis within an atmospheric layer ($\delta x_j = w_x \delta t_j$) [L]; equation (5).
δy_j wind transport of a particle of size j along the y axis within an atmospheric layer ($\delta y_j = w_y \delta t_j$) [L]; equation (5).
δz thickness of each atmospheric layer [L].
ρ_{dep} density of tephra fall deposit [M L^{-3}].
σ_ϕ graphic standard deviation (grain size parameter) [*Inman*, 1952].
$\sigma^2_{i,j}$ variance of the Gaussian mass distribution on the ground of particles of size j released from a point source i [L^2]; equations (6) and (8).
σ_p standard deviation of the Gaussian distribution of the mass in the ascending plume [L]; equation (7).
ϕ granulometric unit: $\phi = -\log_2(10^3 d)$, where d is the particle diameter in m.
$\phi_{\max}$ maximum particle diameter.
$\phi_{\min}$ minimum particle diameter.

[72] **Acknowledgments.** Many thanks to Steve Sahetapy-Engel for his continuous support and sharing of his experience and knowledge of the ∼A.D. 1315 Kaharoa eruption. We also thank Bill Rose and an anonymous reviewer for constructive comments and suggestions. NCEP reanalysis data were provided by the NOAA-CIRES Climate Diagnostics Center, Boulder, Colorado, from their Web site at http://www.cdc.noaa.gov/. This research was funded by a subcontract from the Foundation for Research, Science and Technology via J. W. Cole and the University of Canterbury (New Zealand).

References

Aloisi, M., M. D'Agostino, K. G. Dean, A. Mostaccio, and G. Neri (2002), Satellite analysis and PUFF simulation of the eruptive cloud generated by the Mount Etna paroxysm of 22 July 1998, *J. Geophys. Res.*, *107*(B12), 2373, doi:10.1029/2001JB000630.

Armienti, P., G. Macedonio, and M. T. Pareschi (1988), A numerical-model for simulation of tephra transport and deposition: Applications to May 18, 1980, Mount-St-Helens eruption, *J. Geophys. Res.*, *93*(B6), 6463–6476.

Barberi, F., G. Macedonio, M. T. Pareschi, and R. Santacroce (1990), Mapping the tephra fallout risk: An example from Vesuvius, Italy, *Nature*, *344*, 142–144.

Blong, R. (1994), The Rabaul eruption, 1994, *Aust. Geogr.*, *25*(2), 186–190.

Bonadonna, C., and B. F. Houghton (2005), Total grainsize distribution and volume of tephra-fall deposits, *Bull. Volcanol.*, in press.

Bonadonna, C., and J. C. Phillips (2003), Sedimentation from strong volcanic plumes, *J. Geophys. Res.*, *108*(B7), 2340, doi:10.1029/2002JB002034.

Bonadonna, C., G. G. J. Ernst, and R. S. J. Sparks (1998), Thickness variations and volume estimates of tephra fall deposits: The importance of particle Reynolds number, *J. Volcanol. Geotherm. Res.*, *81*(3–4), 173–187.

Bonadonna, C., G. Macedonio, and R. S. J. Sparks (2002), Numerical modelling of tephra fallout associated with dome collapses and Vulcanian explosions: Application to hazard assessment on Montserrat, in *The Eruption of Soufrière Hills Volcano, Montserrat, From 1995 to 1999*, edited by T. H. Druitt and B. P. Kokelaar, *Geol. Soc. London Mem.*, *21*, 517–537.

Bursik, M. I., S. N. Carey, and R. S. J. Sparks (1992a), A gravity current model for the May 18, 1980 Mount-St-Helens plume, *Geophys. Res. Lett.*, *19*(16), 1663–1666.

Bursik, M. I., R. S. J. Sparks, J. S. Gilbert, and S. N. Carey (1992b), Sedimentation of tephra by volcanic plumes: I. Theory and its comparison with a study of the Fogo A Plinian deposit, Sao Miguel (Azores), *Bull. Volcanol.*, *54*, 329–344.
Canuti, P., N. Casagli, F. Catani, and G. Falorni (2002), Modeling of the Guagua Pichincha volcano (Ecuador) lahars, *Phys. Chem. Earth*, *27*(36), 1587–1599.
Carey, S., and H. Sigurdsson (1987), Temporal variations in column height and magma discharge rate during the 79 AD eruption of Vesuvius, *Geol. Soc. Am Bull.*, *99*(2), 303–314.
Carey, S. N., and H. Sigurdsson (1982), Influence of particle aggregation on deposition of distal tephra from the May 18, 1980, eruption of Mount St-Helens volcano, *J. Geophys. Res.*, *87*(B8), 7061–7072.
Carey, S. N., and H. Sigurdsson (1986), The 1982 eruptions of El Chichon volcano, Mexico (2), Observations and numerical modelling of tephra-fall distribution, *Bull. Volcanol.*, *48*, 127–141.
Carey, S. N., and R. S. J. Sparks (1986), Quantitative models of the fallout and dispersal of tephra from volcanic eruption columns, *Bull. Volcanol.*, *48*, 109–125.
Chhabra, R. P., L. Agarwal, and N. K. Sinha (1999), Drag on non-spherical particles: An evaluation of available methods, *Powder Technol.*, *101*(3), 288–295.
Chung, M. R. (1991), The eruption of Nevado del Ruiz Volcano, Colombia, South America (November 13, 1985), in *Natural Disaster Studies*, edited by N. R. Council, pp. 109, Natl. Acad. Press, Washington, D. C.
Cole, J. W. (1970), Structure and eruptive history of Tarawera Volcanic Complex, *N. Z. J. Geol. Geophys.*, *13*, 879–902.
Coltelli, M., M. Pompilio, P. Del Carlo, S. Calvari, S. Pannucci, and V. Scribano (1998), Etna. Eruptive activity, *Acta Vulcanol.*, *10*(1), 141–148.
Connor, C. B., B. E. Hill, B. Winfrey, N. M. Franklin, and P. C. La Femina (2001), Estimation of volcanic hazards from tephra fallout, *Nat. Hazards Rev.*, *2*(1), 33–42.
Cronin, S. J., M. J. Hedley, V. E. Neall, and R. G. Smith (1998), Agronomic impact of tephra fallout from the 1995 and 1996 Ruapehu Volcano eruptions, New Zealand, *Environ. Geol.*, *34*(1), 21–30.
Di Vito, M. A., R. Isaia, G. Orsi, J. Southon, M. D'Antonio, S. de Vita, L. Pappalardo, and M. Piochi (1999), Volcanism and deformation since 12,000 years at the Campi Flegrei caldera (Italy), *J. Volcanol. Geotherm. Res.*, *91*(2–4), 221–246.
Ernst, G. G. J., R. S. J. Sparks, S. N. Carey, and M. I. Bursik (1996), Sedimentation from turbulent jets and plumes, *J. Geophys. Res.*, *101*(B3), 5575–5589.
Fedotov, S. A., S. T. Balesta, V. N. Dvigalo, A. A. Razina, G. B. Flerov, and A. M. Chirkov (1991), New Tolbachik volcanoes, in *Active Volcanoes of Kamchatka*, edited by O. M. Vanyukova, p. 302, Nauka, Moscow.
Fierstein, J., and W. Hildreth (1992), The Plinian eruptions of 1912 at Novarupta, Katmai National Park, Alaska, *Bull. Volcanol.*, *54*, 646–684.
Glaze, L. S., and S. Self (1991), Ashfall dispersal for the 16 September 1986, eruption of Lascar, Chile, calculated by a turbulent-diffusion model, *Geophys. Res. Lett.*, *18*(7), 1237–1240.
Hanna, S. R., G. A. Briggs, and R. P. Hosker (1982), *Handbook on Atmospheric Diffusion*, 102 pp., Def. Tech. Inf. Cent., U.S. Dep. of Energy, Fort Belvoir, Va.
Heffter, J. L., and B. J. B. Stunder (1993), Volcanic ash forecast transport and dispersion (Vaftad) model, *Weather Forecast.*, *8*(4), 533–541.
Hildreth, W., and R. E. Drake (1992), Volcano Quizapu, Chilean Andes, *Bull. Volcanol.*, *54*, 93–125.
Hill, B. E., C. B. Connor, M. S. Jarzemba, P. C. La Femina, M. Navarro, and W. Strauch (1998), 1995 eruptions of Cerro Negro volcano, Nicaragua, and risk assessment for future eruptions, *Geol. Soc. Am. Bull.*, *110*(10), 1231–1241.
Houtekamer, P. L., and L. Lefaivre (1997), Using ensemble forecasts for model validation, *Mon. Weather Rev.*, *125*(10), 2416–2426.
Hurst, A. W., and R. Turner (1999), Performance of the program ASHFALL for forecasting ashfall during the 1995 and 1996 eruptions of Ruapehu Volcano, *N. Z. J. Geol. Geophys.*, *42*(4), 615–622.
Inman, D. L. (1952), Measures for describing the size distribution of sediments, *J. Sediment. Petrol.*, *22*, 125–145.
Iverson, R. M., S. P. Schilling, and J. W. Vallance (1998), Objective delineation of lahar-inundation hazard zones, *Geol. Soc. Am. Bull.*, *110*, 972–984.
Kalnay, E., et al. (1996), The NCEP/NCAR 40-year reanalysis project, *Bull. Am. Meteorol. Soc.*, *77*(3), 437–471.
Keam, R. F. (1988), *Tarawera: The Volcanic Eruption of 1886*, 472 pp., Auckland, New Zealand.
Kokelaar, B. P. (2002), Setting, chronology and consequences of the eruption of Soufrière Hills Volcano, Montserrat (1995–1999), in *The Eruption of Soufrière Hills Volcano, Montserrat, From 1995 to 1999*, edited by T. H. Druitt and B. P. Kokelaar, *Mem. Geol. Soc. London*, *21*, 1–43.
Koyaguchi, T., and M. Ohno (2001), Reconstruction of eruption column dynamics on the basis of grain size of tephra fall deposits: 1. Methods, *J. Geophys. Res.*, *106*(B4), 6499–6512.
Kunii, D., and O. Levenspiel (1969), *Fluidization Engineering*, John Wiley, New York.
Lacroix, A. (1904), *La Montagne Pelée et ses Eruptions*, Masson, Paris.
Leonard, G. S., J. W. Cole, I. A. Nairn, and S. Self (2002), Basalt triggering of the c. AD 1305 Kaharoa rhyolite eruption, Tarawera Volcanic Complex, New Zealand, *J. Volcanol. Geotherm. Res.*, *115*(3–4), 461–486.
Lowe, D. J., B. G. McFadgen, T. F. G. Higham, A. G. Hogg, P. C. Froggatt, and I. A. Nairn (1998), Radiocarbon age of the Kaharoa Tephra, a key marker for late-Holocene stratigraphy and archaeology in New Zealand, *Holocene*, *8*(4), 487–495.
Macedonio, G., M. T. Pareschi, and R. Santacroce (1988), A numerical simulation of the Plinian fall phase of 79 A.D. eruption of Vesuvius, *J. Geophys. Res.*, *93*(B12), 14,817–14,827.
Maulucci Vivolo, F. P. (1994), Lettere di Plinio il Giovane a Tacito sull'eruzione del Vesuvio (da C. Plini Caecili Secundi Epistularum libri decem), 39 pp., Bastogi Ed. Ital., Foggia, Italy.
Melnik, O. (2000), Dynamics of two-phase conduit flow of high-viscosity gas-saturated magma: Large variations of sustained explosive eruption intensity, *Bull. Volcanol.*, *62*(3), 153–170.
Morton, B., G. L. Taylor, and J. S. Turner (1956), Turbulent gravitational convection from maintained and instantaneous source, *Proc. R. Soc. London*, *234*, 1–23.
Nairn, I. A. (1989), Sheet V16AC-Tarawera: Geological map of New Zealand, scale 1:50,000, Dep. of Sci. and Ind. Res., Wellington.
Nairn, I. A., S. Self, J. W. Cole, G. S. Leonard, and C. Scutter (2001), Distribution, stratigraphy, and history of proximal deposits from the c. AD 1305 Kaharoa eruptive episode at Tarawera Volcano, New Zealand, *N. Z. J. Geol. Geophys.*, *44*(3), 467–484.
Nairn, I. A., P. R. Shane, J. W. Cole, G. J. Leonard, S. Self, and N. Pearson (2004), Rhyolite magma processes of the similar to AD 1315 Kaharoa eruption episode, Tarawera volcano, New Zealand, *J. Volcanol. Geotherm. Res.*, *131*(3–4), 265–294.
Newhall, C. G., and R. P. Hoblitt (2002), Constructing event trees for volcanic crises, *Bull. Volcanol.*, *64*, 3–20.
Palmer, T. N. (2000), Predicting uncertainty in forecasts of weather and climate, *Rep. Progr. Phys.*, *63*(2), 71–116.
Pasquill, F. (1974), *Atmospheric Diffusion*, John Wiley, New York.
Pinel, V., and C. Jaupart (2003), Magma chamber behavior beneath a volcanic edifice, *J. Geophys. Res.*, *108*(B2), 2072, doi:10.1029/2002JB001751.
Prata, A. J., and I. F. Grant (2001), Retrieval of microphysical and morphological properties of volcanic ash plumes from satellite data: Application to Mt. Ruapehu, New Zealand, *Q. J. R. Meteorol. Soc.*, *127*(576), 2153–2179.
Pyle, D. M. (1989), The thickness, volume and grainsize of tephra fall deposits, *Bull. Volcanol.*, *51*(1), 1–15.
Riley, C. M., W. I. Rose, and G. J. S. Bluth (2003), Quantitative shape measurements of distal volcanic ash, *J. Geophys. Res.*, *108*(B10), 2504, doi:10.1029/2001JB000818.
Rout, D. J., J. Cassidy, C. A. Locke, and I. E. M. Smith (1993), Geophysical evidence for temporal and structural relationships within the Monogenetic basalt volcanoes of the Auckland Volcanic Field, northern New-Zealand, *J. Volcanol. Geotherm. Res.*, *57*(1–2), 71–83.
Sahetapy-Engel, S. (2002), Tephra fall deposit of the AD 1305 eruption of Tarawera, New Zealand: Reconstruction of eruption dynamics, Master thesis, Univ. of Hawaii, Honolulu.
Scasso, R., H. Corbella, and P. Tiberi (1994), Sedimentological analysis of the tephra from 12–15 August 1991 eruption of Hudson Volcano, *Bull. Volcanol.*, *56*, 121–132.
Searcy, C., K. Dean, and W. Stringer (1998), PUFF: A high-resolution volcanic ash tracking model, *J. Volcanol. Geotherm. Res.*, *80*(1–2), 1–16.
Sparks, R. S. J., and L. Wilson (1982), Explosive volcanic eruptions: V. Observations of plume dynamics during the 1979 Soufrière eruption, St. Vincent, *Geophys. J. R. Astron. Soc.*, *69*, 551–570.
Sparks, R. S. J., and S. R. Young (2002), The eruption of Soufrière Hills Volcano, Montserrat (1995–1998), Overview of scientific results, in *The Eruption of Soufrière Hills Volcano, Montserrat, From 1995 to 1999*, edited by T. H. Druitt and B. P. Kokelaar, *Mem. Geol. Soc. London*, *21*, 45–69.
Sparks, R. S. J., L. Wilson, and H. Sigurdsson (1981), The pyroclastic deposits of the 1875 eruption of Askja, Iceland, *Philos. Trans. R. Soc. London*, *229*, 241–273.
Sparks, R. S. J., M. I. Bursik, G. J. Ablay, R. M. E. Thomas, and S. N. Carey (1992), Sedimentation of tephra by volcanic plumes: 2. Controls

on thickness and grain-size variations of tephra fall deposits, *Bull. Volcanol.*, *54*(8), 685–695.
Sparks, R. S. J., M. I. Bursik, S. N. Carey, J. S. Gilbert, L. S. Glaze, H. Sigurdsson, and A. W. Woods (1997), *Volcanic Plumes*, 574 pp., John Wiley, New York.
Sterling, T. L., J. Salmon, D. J. Becker, and D. F. Savarese (1999), *How to Build a Beowulf—A Guide to Implementation and Application of PC Clusters*, 239 pp., MIT Press, Cambridge, Mass.
Stirling, M. W., and C. J. N. Wilson (2002), Development of a volcanic hazard model for New Zealand: First approaches from the methods of probabilistic seismic hazard analysis, *Bull. N. Z. Soc. Earthquake Eng.*, *35*(4), 266–277.
Suzuki, T. (1983), A theoretical model for dispersion of tephra, in *Arc Volcanism, Physics and Tectonics*, edited by D. Shimozuru and I. Yokoyama, pp. 95–113, Terra Sci., Tokyo.
Wadge, G., P. Jackson, S. M. Bower, A. W. Woods, and E. Calder (1998), Computer simulations of pyroclastic flows from dome collapse, *Geophys. Res. Lett.*, *25*(19), 3677–3680.
Walker, G. P. L. (1980), The Taupo Pumice: Product of the most powerful known (ultraplinian) eruption?, *J. Volcanol. Geotherm. Res.*, *8*, 69–94.
Walker, G. P. L. (1981), The Waimihia and Hatepe Plinian deposits from the rhyolitic Taupo Volcanic Centre, *N. Z. J. Geol. Geophys.*, *24*, 305–324.
Walker, G. P. L., S. Self, and L. Wilson (1984), Tarawera, 1886, New Zealand—A basaltic Plinian fissure eruption, *J. Volcanol. Geotherm. Res.*, *21*, 61–78.
Williams, H. (1950), Volcanoes of the Paricutin region, *U.S. Geol. Surv. Bull.*, *965*(B), 165–275.
Woo, G. (2000), *The Mathematics of Natural Catastrophes*, 292 pp., Imperial College Press, London.
Woods, A. W. (1988), The fluid-dynamics and thermodynamics of eruption columns, *Bull. Volcanol.*, *50*(3), 169–193.
Woods, W. (1995), The dynamics of explosive volcanic eruptions, *Rev. Geophys.*, *33*(4), 495–530.

C. Bonadonna, M. Byrne, C. B. Connor, L. Connor, and A. Laing, Department of Geology, University of South Florida, Tampa, FL 33620, USA. (costanza@cas.usf.edu)

T. K. Hincks, Department of Earth Sciences, University of Bristol, Bristol, BS8 1RJ, UK.

B. F. Houghton, Department of Geology and Geophysics, University of Hawaii, Honolulu, HI 96822, USA.